

## THE MYSTERIOUS MERGER OF NGC 6868 AND NGC 6861 IN THE TELESCOPIUM GROUP

M. E. MACHACEK, E. O'SULLIVAN, S. W. RANDALL, C. JONES, AND W. R. FORMAN

Harvard-Smithsonian Center for Astrophysics  
60 Garden Street, Cambridge, MA 02138 USA

*Draft version November 13, 2018*

### ABSTRACT

We use *Chandra* X-ray observations of the hot gas in and around NGC 6868 and NGC 6861 in the Telescopium galaxy group (AS0851) to probe the interaction history between these galaxies. Mean surface brightness profiles for NGC 6868 and NGC 6861 are each well described by double  $\beta$ -models, suggesting that they are each the dominant galaxy in a galaxy subgroup about to merge. Surface brightness and temperature maps of the brightest group galaxy NGC 6868 show a cold front edge  $\sim 23$  kpc to the north, and a cool 0.62 keV spiral-shaped tail to the south. Analysis of the temperature and density across the cold front constrains the relative motion between NGC 6868 and the ambient group gas to be at most transonic; while the spiral morphology of the tail strongly suggests that the cold front edge and tail are the result of gas sloshing due to the subgroup merger. The cooler central region of NGC 6861 is surrounded by a sheath of hot gas to the east and hot, bifurcated tails of X-ray emission to the west and northwest. We discuss supersonic infall of the NGC 6861 subgroup, sloshing from the NGC 6868 and NGC 6861 subgroup merger, and AGN heating as possible explanations for these features, and discuss possible scenarios that may contribute to the order of magnitude discrepancy between the Margorrian and black hole mass -  $\sigma$  predictions for its central black hole.

*Subject headings:* galaxies: clusters: general – galaxies: individual (NGC 6868, NGC 6861) – galaxies: intergalactic medium – X-rays: galaxies

### 1. INTRODUCTION

One of the most important questions facing models of galaxy evolution today is how central supermassive black holes, found at the centers of most galaxies, co-evolve with their host galaxies. The observed correlations between central black hole mass and stellar velocity dispersion in present epoch galaxies ( $M_{\text{BH}} - \sigma_*$ , Gebhardt et al. 2000; Ferrarese & Merrit 2000; Tremaine et al. 2002) and between black hole mass and galaxy bulge mass or bulge luminosity ( $M_{\text{BH}} - M_{\text{bulge}}$ ; Magorrian et al. 1998; Häring & Rix 2004) provide striking evidence for this coevolution. However, the shapes of these correlations, particularly at the extremes of velocity dispersion or luminosity, are not well known, and, which, if either, of these correlations is a reliable predictor of black hole mass in galaxies with high central stellar velocity dispersion or large luminosity remains controversial (Lauer et al. 2007). Key to resolving this controversy is understanding the dynamical connections between galaxy interactions, the feedback cycle from active galactic nuclei (AGNs), and black hole fueling and growth.

Recent observations show that galaxy evolution occurs predominantly in moderately massive galaxy groups at redshifts  $\gtrsim 1$  (Cooper et al. 2006). Thus to build dynamical models for the transformation of galaxies and the growth of their central black holes, we must understand how galaxy interactions and feedback affect gas in and surrounding galaxies in the group environment. Questions that remain poorly understood include: What dynamical processes control the mass and energy flows into or out of the merging galaxies either fueling the central AGN and/or initiating star formation, or quenching star formation and heating and enriching the intragroup medium (IGM)? When and how are the dark matter and hot gas halos of the merging galaxy separated from the galaxy to become part of the group gravitational potential? How efficiently are the outer stellar halos of interacting galaxies stripped? Are central stellar velocity dispersions of

the galaxies affected by these interactions and on what dynamical timescales? What role do non-hydrostatic group gas (IGM) motions, induced by galaxies and galaxy subgroups passing through the group core, play in the co-evolution of the system?

Merging galaxies in nearby galaxy groups are particularly important laboratories in which to address these questions, since only in these groups do X-ray observations have sufficient angular resolution to directly observe the X-ray edges, outflows, cavities, shocks, ripples and tails characteristic of the dynamical processes at work on the galaxies and within the group. Measurements of temperatures and densities in these features allow us to constrain the velocities, orbits and interaction history of the galaxies, as well as probe the cycle of nuclear activity that transports matter and energy between the galaxy's nucleus and the surrounding gas. Modeling the effects of these interactions on nearby galaxies, that lie on the extremes of the black hole mass scaling relations, provides a unique opportunity to understand the galactic processes that determine the shape and validity of these relations.

In this paper we present the results of *Chandra* observations of the two brightest elliptical galaxies, NGC 6868 and NGC 6861, in the Telescopium group (AS0851). AS0851, shown in Figure 1, is an Abell class 0 galaxy group 28 Mpc distant (Tonry et al. 2001), containing  $> 11$  member galaxies (Garcia 1993). Both the brightest group member, elliptical galaxy NGC 6868 ( $20^{\text{h}}09^{\text{m}}54.1^{\text{s}}, -48^{\circ}22'46''.4$ ,  $B_T = 11.66$ , NED) and the second brightest group galaxy, SA0 galaxy NGC 6861 ( $20^{\text{h}}07^{\text{m}}19.5^{\text{s}}, -48^{\circ}22'12''.8$ ,  $B_T = 12.12$ , NED),  $25'.7$  to the west, show signs of recent interactions and are likely to merge. Surprisingly, Wegner et al. (2003) measured a central stellar velocity dispersion of the less luminous galaxy (NGC 6861) of  $\sim 414 \text{ km s}^{-1}$ , a factor 1.6 greater than the  $250 \text{ km s}^{-1}$  central stellar velocity dispersion of the more luminous elliptical galaxy NGC 6868.

We summarize the galaxy properties and estimates of the

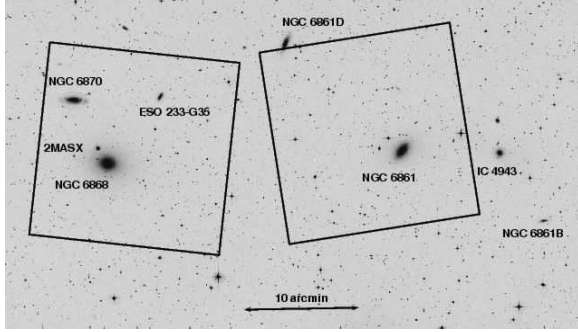


FIG. 1.— Bj-band image of the Telescopium (AS0851) group with the brightest group galaxy NGC 6868 to the left and second brightest group galaxy NGC 6861 to the right. Other bright members of AS0851 are also labeled. Squares show the *Chandra* ACIS-I fields-of-view (FOVs) for the observations discussed in this work. North is up and East is to the left.

central black hole masses for both NGC 6868 and NGC 6861 in Table 1. Using the  $250 \text{ km s}^{-1}$  central stellar velocity dispersion for NGC 6868 in the black hole mass - stellar velocity dispersion ( $M_{BH} - \sigma_*$ ) relation,

$$\log\left(\frac{M_{BH}}{M_\odot}\right) = (8.13 \pm 0.06) + (4.02 \pm 0.32) \log\left(\frac{\sigma_*}{200 \text{ km s}^{-1}}\right), \quad (1)$$

where  $M_{BH}$  is the mass of the black hole and  $\sigma_*$  is the central stellar velocity dispersion (Tremaine et al. 2002; Ferrarese & Merrit 2000; Gephardt et al. 2000), we infer a central black hole mass in NGC 6868 of  $\sim 3.3 \times 10^8 M_\odot$ , typical for black hole masses in elliptical galaxies in groups (see, e.g. Tremaine et al. 2002, Verdoes Kleijn et al. 2006). An alternative estimator, the Magorrian relation, relates the mass of the central black hole  $M_{BH}$  to the stellar mass  $M_*$  of the galaxy’s bulge (as stated in Häring and Rix 2004; see also Magorrian et al. 1998; Marconi & Hunt 2003),

$$\log\left(\frac{M_{BH}}{M_\odot}\right) = (8.20 \pm 0.10) + (1.12 \pm 0.06) \log\left(\frac{M_*}{10^{11} M_\odot}\right). \quad (2)$$

For elliptical and spheroidal galaxies the bulge mass is replaced with the total stellar mass of the galaxy. Following Gilfanov (2004), we use the 2MASS total K-band luminosity of NGC 6868 to estimate the total stellar mass for NGC 6868 in eq. 2 and find  $M_{BH} = 3.1 \times 10^8 M_\odot$ , in excellent agreement with the  $M_{BH} - \sigma_*$  relation.

Optical measurements of NGC 6868 reveal a central dust lane with weak spiral features (Buson et al. 1993, Veron-Cetty & Veron 1988, Hansen et al. 1991), and indicate that gas at the center of the galaxy is not moving in regular orbits (Zeilinger et al. 1996). IRAS measurements of NGC 6868 at 60 and  $100 \mu\text{m}$  confirm the presence of cold dust in the galaxy (Bregman et al. 1998). A possible explanation for these dust features and unusual stellar kinematics is that NGC 6868 has recently captured a dust rich companion. Such a cold gas rich merger could fuel AGN activity and/or black hole growth (Hardcastle et al. 2007; Machacek et al. 2008). NGC 6868 has been observed in the radio at 2.3, 5, and 8.4 GHz with the Parkes and Australian Telescopes (Slee et al. 1994) and at 843 MHz in the SUMSS survey (Mauch et al. 2003). The galaxy is classified as a low-power, flat spectrum ( $\alpha \sim 0.07$ ) radio source with total flux densities of 139 mJy, and 124 mJy at 843 MHz and 5 GHz, respectively. The brightness temperature and spectral slope are inconsistent with thermal emission

from star forming HII regions, such that the source of the radio emission is likely an active galactic nucleus.

On the other hand, the  $\sim 400 \text{ km s}^{-1}$  central velocity dispersion for NGC 6861, located  $\sim 206 \text{ kpc}$  away from NGC 6868, is one of the highest measured for any early type galaxy (Wegner et al. 2003; Koprolin & Zeilinger 2000). From the  $M_{BH} - \sigma_*$  relation (eq. 1), we infer a supermassive black hole in NGC 6861 of  $\sim 2.5 \times 10^9 M_\odot$ , similar to that in M87, the central dominant giant elliptical galaxy in the Virgo galaxy cluster, and to that in NGC 4649, a giant elliptical galaxy also in Virgo (Tremaine et al. 2002). This is an order of magnitude higher than the  $2.1 \times 10^8 M_\odot$  black hole mass expected for NGC 6861 from the Magorrian relation (eq. 2).

The dispersion velocity for gas in the inner 30–50 pc of NGC 6861, close to the black hole sphere of influence, has been measured using central emission line widths from Hubble Space Telescope STIS data (Verdoes Kleijn et al. 2006; Beifiori et al. 2009). Both groups confined their analysis to galaxies that did not show unusually disturbed stellar kinematics. In each case the measured central gas velocity for NGC 6861 is among the highest in their samples, comparable or exceeding that found in NGC 4486 (M87). However, extracting the black hole mass from the measured gas dispersions is highly sensitive to the assumed morphology of the gas and, for the thin disk models used by these authors, the unknown inclination of the central gas disk. Beifiori et al. (2009) argue that the data are consistent with a range of black hole masses, i.e.  $\sim 1.5 \times 10^9 M_\odot$  for disk inclination angle  $i = 33^\circ$  to  $3.6 \times 10^8 M_\odot$  for  $i = 81^\circ$ , that within the uncertainties of the scaling relations, span the predictions of either the Magorrian or  $M_{BH} - \sigma_*$  relation.

These data suggest several possible scenarios. The black hole mass for NGC 6861 may be high, as suggested by the  $M_{BH} - \sigma_*$  relation, and NGC 6861 may itself be the central galaxy in a massive subgroup dark matter halo merging with the NGC 6868 subgroup. Alternatively, the high central gas velocity dispersion in NGC 6861 could be caused, in part, by the input of kinetic energy into the gas from the central AGN through outflows or turbulence (Verdoes Kleijn et al. 2006; Capellari et al. 2000). Then the mass of the central black hole needed to explain the high central gas velocities could be smaller, falling below the  $M_{BH} - \sigma_*$  prediction and closer to that of the Magorrian relation (eq. 2). NGC 6861 does host a weak radio source, with core radio power, measured with the Australian Telescope, of 6 mJy at 5 GHz (Slee et al. 1994). The radio source is extended with a core-to-total radio power ratio of  $\sim 0.25$ . Although there is no evidence for large scale radio jets, the  $5''$  (0.7 kpc) angular resolution of the Australian Telescope does not rule out substructure on scales of a few tens of parsecs nor preclude feedback from previous episodes of AGN activity, each of which might heat the central interstellar medium (ISM), lowering the black hole mass required to model the central gas velocity dispersions observed with STIS. Finally, the stellar velocity dispersion of NGC 6861 could be anomalously high due to gravitational interactions with NGC 6868 or other group galaxies. In these latter two cases, the puzzle is then what interaction history could cause such a high stellar velocity dispersion for NGC 6861, while not producing obviously unrelaxed stellar kinematics that would have excluded the galaxy from the Beifiori et al. (2009) and Verdoes Kleijn et al. (2006) samples.

NGC 6868 and NGC 6861 have been observed in X-rays with both the *ROSAT* and *Chandra* X-ray Observatories.

These observations have been used to measure total X-ray luminosities and test X-ray scaling laws (Beuing et al. 1999, O’Sullivan et al. 2001, Ellis & O’Sullivan 2006) and also to determine average density and temperature profiles for the galaxies (Fukazawa et al. 2006). In this paper we use the *Chandra* X-ray measurements of the density and temperature distribution of hot gas in NGC 6868, NGC 6861, and in the AS0851 group core to investigate the interaction history of these galaxies and how those interactions may affect nuclear activity and black hole growth. Our discussion is organized as follows: In §2 we review the *Chandra* observations and our data reduction and processing procedures. In §3 we discuss the mean X-ray surface brightness around each galaxy and search for substructure in the AS0851 group. In §4 we analyse density and temperature features observed in these data and how they may constrain possible interaction scenarios between the galaxies and group IGM. In §5 we comment on how these interactions may impact the black hole mass relations. We summarize our results in §6. Unless otherwise indicated, quoted uncertainties are 90% confidence levels for spectral parameters and  $1\sigma$  uncertainties for X-ray counts. Coordinates are J2000. We adopt a luminosity distance of 28 Mpc, obtained from surface brightness fluctuation measurements of NGC 6868 (Tonry et al. 2001), as representative of the distance to the core of the AS0851 galaxy group and to NGC 6861. Assuming the five year WMAP values for cosmological parameters ( $\Omega_m = 0.27$ ,  $\Omega_\lambda = 0.73$ ,  $H_0 = 0.71$ ; Hinshaw et al. 2009),  $1''$  at 28 Mpc corresponds to a distance of 0.134 kpc in the plane of the sky.

## 2. CHANDRA OBSERVATIONS AND DATA REDUCTION

NGC 6868 was observed for 23.5 ks on 2002 January 11 (Obsid 3191) and NGC 6861 for 22.8 ks on 2002 July 26 (Obsid 3190), each with the Advanced CCD Imaging Spectrometer - Imaging Array (ACIS-I; Gamire et al. 1992, Bautz et al. 1998) in VFaint mode on board the *Chandra* X-ray Observatory. We used the standard X-ray analysis packages from CIAO3.4 and FTOOLS for image processing and spectral extraction and XSPEC11.3.0 for spectral modeling. The data were initially filtered to reject bad grades (1,5,7) and data that fell on hot pixels. Data flagged in VFaint mode as having excessive count rates in the border pixels surrounding event islands were also removed to optimize signal to noise at energies below 1 keV, where most of the source emission is expected for these galaxies. We then reprocessed the data and created exposure maps and response files applying the most recent gain tables and instrumental corrections, including corrections for the charge transfer inefficiency on the ACIS-I CCDs, the time-dependent build-up of contaminants on the optical filter, and the secular drift of the average pulse-height amplitude for photons of fixed energy.<sup>1</sup> The data were cleaned using a  $3\sigma$  clipping algorithm in the script `lc_clean` to remove periods of anomalously high and low count rates. Inspection of the resulting light curves showed that this was adequate for OBSID 3191, resulting in a useful exposure of 21551 s for that observation. However, inspection of the light curves for OBSID 3190 (NGC 6861) showed that contamination from a strong particle flare (ringing) persisted throughout the latter half of the observation. Thus we used only the pre-flare data from OBSID 3190 in our analysis, resulting in a useful exposure of 9852 s for NGC 6861.

<sup>1</sup> see, <http://cxc.harvard.edu/contrib/alexey/tgain/tgain.html>

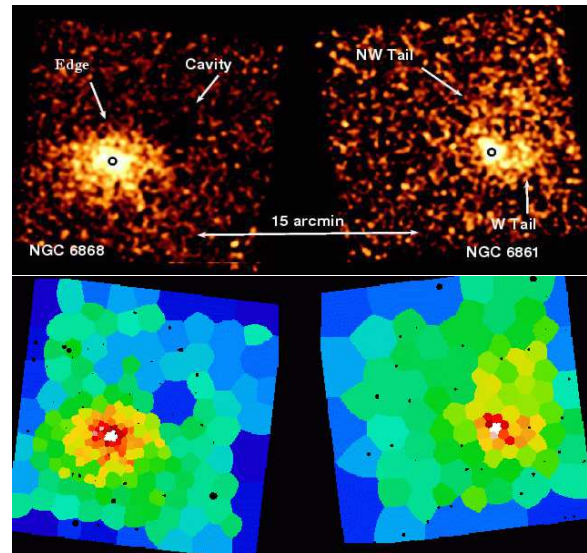


FIG. 2.— (upper) 0.5–2 keV *Chandra* mosaic of diffuse emission in NGC 6868 and NGC 6861 in the AS0851 galaxy group. Point sources have been excluded and the resulting image has been background-subtracted, exposure corrected and smoothed with an  $8''$  Gaussian kernel. 1 pixel =  $1''.968 \times 1''.968$ . Circles indicate the galaxy centers. North is up and east is to the left. (lower) 0.5–2 keV image of NGC 6868 and NGC 6861 adaptively binned using Voronoi tessellation, with  $3''.936 \times 3''.936$  pixels and  $S/N = 5$ , to highlight the fainter structures.

Backgrounds for the imaging analysis and for spectral analysis of the IGM were constructed from the  $1.5 \times 10^6$  s source free background data set<sup>2</sup> appropriate for our observation dates and instrument configuration. Background data sets for each observation were normalized by comparing count rates in the 9.0–11.5 keV energy band, where particle background dominates. This resulted in additional normalization factors of 0.98 and 1.07 for the backgrounds for OBSID 3191 and OBSID 3190, respectively. We identified X-ray point sources in each observation in the 0.3–7 keV energy band using a wavelet decomposition algorithm with a  $5\sigma$  detection threshold. Using 10 photon counts, we identify point sources to limiting 0.3–7 keV fluxes of  $8.6 \times 10^{-15}$  erg s<sup>-1</sup> and  $4.3 \times 10^{-15}$  erg s<sup>-1</sup> for OSID 3190 (NGC 6861) and OSID 3191 (NGC 6868), respectively. Since we are interested in the properties of the diffuse X-ray emission and possible AGN activity, X-ray point sources, other than the galaxies’ nuclei, were removed from all subsequent analyses.

## 3. MEAN SURFACE BRIGHTNESS PROFILES AND GROUP STRUCTURE

In the upper panel of Figure 2 we show a mosaiced 0.5–2 keV *Chandra* image of the diffuse emission surrounding NGC 6868 (left) and NGC 6861 (right) in the galaxy group AS0851. The image has been background subtracted and exposure corrected, and, after exclusion of X-ray point sources, has been smoothed with an  $8''$  Gaussian kernel. In the lower panel of Figure 2 we present an adaptively binned 0.5–2 keV *Chandra* image of the same regions, using the Voronoi tessellation technique with a signal-to-noise ( $S/N$ ) of 5 to highlight faint emission features. We first construct mean surface brightness profiles for NGC 6868, NGC 6861 and the surrounding gas to understand the structure of the group as

<sup>2</sup> see <http://cxc.harvard.edu/contrib/maxim/acisbg>

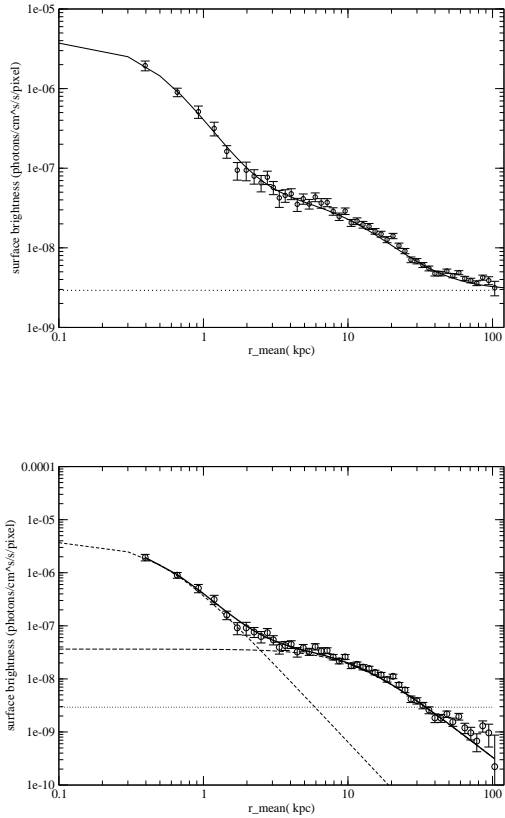


FIG. 3.— (*upper*) Azimuthally averaged 0.5–2 keV radial surface brightness profile of NGC 6868 constructed using concentric circular annuli, centered on NGC 6868’s nucleus, with logarithmically increasing width. The solid line denotes the sum of the double  $\beta$ -model shown in the lower panel and a constant ( $7.5 \times 10^{-10}$  photons  $\text{cm}^{-2}$  arcsec $^{-2}$ , dotted line) residual soft Galactic X-ray background. (*lower*) The azimuthally averaged surface brightness profile of NGC 6868 from the upper panel after subtraction of the soft Galactic X-ray component (dotted line). The solid line is the sum of two  $\beta$ -models (shown as dashed lines), an inner model with index  $\beta = 0.65$  and core radius  $r_c = 0.492$  kpc and an outer model with  $\beta = 0.52$  and  $r_c = 11$  kpc. The dotted line denotes the constant soft background level and thus when signal-to-noise  $S/N = 1$ .

a whole and search for evidence of substructure in AS0851 that might signal the merger of two subgroups. In the following section (§4), we will discuss the evidence for interactions suggested by the surface brightness features identified in Figure 2 in and around each galaxy.

### 3.1. NGC 6868

In Figure 3 (open circles, upper panel) we show the mean radial surface brightness profile for NGC 6868 constructed using concentric circular annuli of logarithmically increasing width, centered on NGC 6868’s nucleus. The profile flattens at large radii indicative of a residual soft X-ray background component in the data. ROSAT All Sky Image (RASS) maps confirm that NGC 6868 and NGC 6861 lie in a region of enhanced soft Galactic X-ray emission. Since this soft Galactic X-ray background is expected to be constant over the field of view, we estimate this background using the mean 0.5–2 keV emission in the S2 CCD from OBSID 3190, the most distant ( $r_{\text{mean}} \sim 180$  kpc) source free region from

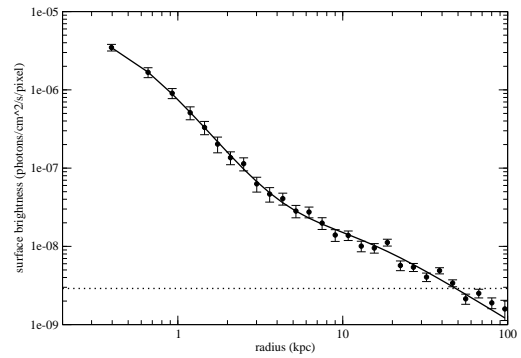
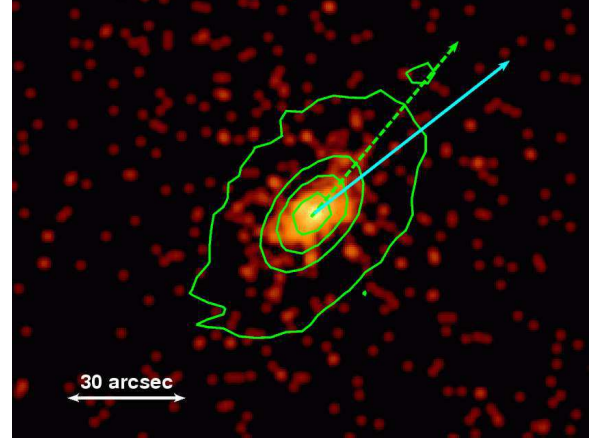


FIG. 4.— (*upper*) 0.5–2 keV *Chandra* X-ray image of the bright inner emission region of NGC 6861 with 2MASS K-band contours superposed. Resolved point sources have been excluded and the image has been smoothed with a  $\sigma = 0''.984$  Gaussian kernel. K band contour levels are 560, 580, 610, 720 data units, respectively. The dashed arrow shows the 2MASS K band position angle ( $-40^\circ$  counter-clockwise from North), while the solid arrow is the position angle ( $-52^\circ \pm 7^\circ$ ) determined from the elliptical  $\beta$ -model fit ( $\beta = 0.62, r_c = 0.62$  kpc,  $e = 0.4$ ) to the 0.5–2 keV X-ray surface brightness profile within 7.3 kpc ( $54''$ ) of NGC 6861. 1 pixel =  $0''.492 \times 0''.492$ . (*lower*) Azimuthally averaged surface brightness profile of NGC 6861 to large radii. Solid line denotes the double spherical  $\beta$ -model fit where  $\beta = 0.61(0.38)$  and  $r_c = 0.5(11.9)$  kpc for the inner (outer)  $\beta$ -model component, respectively.)

NGC 6868, where we expect the soft Galactic background to dominate. We find the soft Galactic background level to be  $7.5 \times 10^{-10}$  photons  $\text{cm}^{-2}$  arcsec $^{-2}$  and denote this level as the horizontal dotted line in both panels of Figure 3. In the lower panel of Figure 3 we show the surface brightness profile for NGC 6868 in the 0.5–2 keV energy after subtraction of this residual soft Galactic background. The mean surface brightness profile is well parameterized by the sum of two  $\beta$ -models, an inner  $\beta$ -model with  $\beta = 0.65$  and core radius  $r_c = 0.49$  kpc, and an outer  $\beta$ -model with  $\beta = 0.52$  and  $r_c = 11$  kpc. Note that beyond  $r \sim 35$  kpc the fit becomes highly uncertain since the soft Galactic background dominates the faint group emission in this energy band.

### 3.2. NGC 6861

The distribution of starlight in NGC 6861 is highly eccentric (see Fig. 1). From 2MASS K band measurements, the ellipticity ( $e = 1 - b/a$ ) within the “total” K-band isophotal semi-major radius  $a = 97''.4$  (13 kpc) is 0.4 with posi-

tion angle, measured counter-clockwise from north (J2000) of  $140^\circ$  (NED). The brightest X-ray emission, shown in Figure 4, is also eccentric and highly compact. Using the CIAO tool *Sherpa* to fit a single two-dimensional elliptical  $\beta$ -model plus constant background to this central emission for  $r \leq 54''$  (7.3 kpc), we find an eccentricity  $0.40 \pm 0.04$ , consistent with that of the starlight, but with position angle  $128^\circ \pm 7^\circ$ , twisted by less than  $2\sigma$  relative to position angle measured for the stellar light. We find  $\beta = 0.62^{+0.02}_{-0.01}$  and a core radius  $r_c = 0.62^{+0.06}_{-0.03}$  kpc, similar to elliptical beta model fits to other elliptical galaxies in galaxy groups (Osmond & Ponman 2004). As we increase the fit radius to include fainter emission, the eccentricity decreases ( $e = 0.19 \pm 0.05$  for  $r \leq 42$  kpc), as expected as we include emission from gas residing in the more spherical gravitational potential of the group or subgroup. To separate the possible subgroup emission from the galaxy component, we fit the background-subtracted, azimuthally-averaged surface brightness profile, shown in Figure 4, with the sum of two spherically symmetric beta models (as we did for NGC6868 in §3.1). The soft Galactic background denoted by the dashed line in Figure 4 has also been subtracted. We find  $(\beta, r_c)$  of (0.61, 0.5 kpc) for the inner (galactic) component and (0.38, 11.9 kpc) for the extended (associated subgroup) component. The extended component  $\beta$  parameter for NGC 6861 is much shallower than that found for NGC 6868, but still falls within the range of  $\beta$  parameters ( $0.36 \leq \beta \leq 0.58$ ) found for the extended X-ray components around elliptical galaxies in groups in the GEMS survey (Osmond & Ponman 2004).

### 3.3. Group Structure

The fact that the surface brightness distribution in and around NGC 6868 and NGC 6861, the two brightest galaxies in AS0851, are both described by double  $\beta$ -models suggests that these galaxies may be the dominant galaxies in two subgroups that are merging. To investigate whether there is evidence for subgroup substructure in the radial velocity distribution of galaxies in the AS0851 group, we identify all galaxies with measured radial velocities  $2000 < v_r < 4000 \text{ km s}^{-1}$  within  $4^\circ$  (2 Mpc) of the brightest group galaxy NGC 6868 (NED; Huchra & Geller, CfA Redshift Survey 2008).<sup>3</sup> We find 46 galaxies, with radial velocities closely grouped between  $2400 < v_r < 3700 \text{ km s}^{-1}$  and well removed in redshift from prominent, background large scale filaments at  $v_r \sim 5000 \text{ km s}^{-1}$  that appear nearby in projection (see the upper left panel of Fig. 5). Using the method of Osmond & Ponman (2004), we find a velocity dispersion for these 46 galaxies of  $274 \pm 29 \text{ km s}^{-1}$ . While this velocity dispersion is typical of that expected for a cool 1 keV group, the spatial extent is much larger, i.e.  $r_{500}$  is expected to be only  $\sim 0.6$  Mpc for a 1 keV group (Osmond & Ponman 2004), which may argue in favor of the merger of two cool galaxy subgroups. However, as seen in the lower left panel of Figure 5, there is little evidence for substructure in radial velocity space even on these larger scales. 65% of the galaxies in this sample (30 of 46) are clustered within 1 Mpc of NGC 6868 or NGC 6861 and 52% (24 galaxies) are within  $r_{500}$  (0.6 Mpc) of NGC 6868. The group velocity dispersion of galaxies within 2 Mpc, 1 Mpc and 0.6 Mpc ( $274 \pm 29 \text{ km s}^{-1}$ ,  $263 \pm 34 \text{ km s}^{-1}$ , and  $251 \pm 37 \text{ km s}^{-1}$ , respectively) all agree within errors. NGC 6868 and NGC 6861 have radial velocities separated by only  $35 \text{ km s}^{-1}$  and both radial velocities lie

close to the median radial velocity of the galaxy sample as a whole ( $\sim 2853 \text{ km s}^{-1}$ ). Thus the merger of the NGC 6868 and NGC 6861 subgroups is predominantly in the plane of the sky, and it is unclear which subgroup, if either, may be at the center of the AS0851 group potential.

## 4. EVIDENCE FOR INTERACTIONS

Galaxy interactions and the dynamical evolution of the surrounding IGM are revealed through asymmetries in the density and temperature of the gas. When the relative motion between the galaxy or subgroup gas halo and any ambient medium lies close to the plane of the sky, we expect ram pressure acting on the infalling body to produce a sharp X-ray surface brightness discontinuity along the leading ‘edge’ of the infall trajectory, associated with a cold front, as well as a trailing tail or wake of stripped galaxy or subgroup gas (see, e.g. Forman et al. 1979, Rangarajan et al. 1995, Randall et al. 2008 for M86; Scharf et al. 2004, Machacek et al. 2005a for NGC 1404; Machacek et al. 2006 for NGC 4552). The surface brightness morphology of the gas around NGC 6868 suggests motion. In particular, the surface brightness distribution around NGC 6868, shown in Figure 2, appears flattened to the north, with a sharp discontinuity (edge) to the north and west. X-ray emission from NGC 6868 is more extended (tail-like) to the south and east. Other asymmetries in the surface brightness distribution include a bright clump of emission  $\sim 1'$  (8 kpc) to the east of the nucleus, and a roughly spherical deficit in surface brightness in the IGM to the northwest of NGC 6868, as well as a partial rim-like feature in the ISM gas to the southwest. These latter features may be evidence for X-ray cavities inflated by prior AGN activity.

Although the brightest X-ray emission in NGC 6861 follows the optical isophotes, it is extremely compact for a massive galaxy and the asymmetries in the X-ray surface brightness revealed at larger radii are striking (see Figs. 2 and 6). An approximately  $3'$  (24 kpc) long X-ray tail (W Tail) extends due west of NGC 6861. A plume of emission rises  $70''$  (9.4 kpc) to the northeast, perpendicular to the major axis of the galaxy, and a tail of X-ray emission trails NGC 6861 to the northwest (NW tail).

Several scenarios offer possible explanations for the distorted surface brightness morphologies observed in and around NGC 6868 and NGC 6861. First, NGC 6868, NGC 6861 or both galaxies may be moving with respect to the group IGM, such that the extended tail-like features may be the result of ram pressure (Gunn & Gott 1972) and/or turbulent-viscous (Nulsen 1982; Quilis et al. 2000) stripping of galaxy gas, or gravitational focusing of the group IGM (Bondi & Hoyle 1944; Bondi 1952; Ruderman & Spiegel 1971; Machacek et al. 2005b). Second, we may be witnessing a more evolved merger of two massive subgroups whose dominant galaxies are NGC 6868 and NGC 6861, respectively, such that much of the NGC 6861’s outer stellar halo and subgroup gas has been tidally stripped after multiple passes through the core of AS0851 (Byrd & Valtonen 1990; Moore et al. 1996) and the group IGM set in motion and mixed as a result of these gravitational encounters (sloshing, see, e.g., Markevitch et al. 2001; Mazzotta et al. 2003; Tittley & Henriksen 2005; Ascasibar & Markevitch 2006). Third, the disturbed morphologies may partly be the result of energetic outbursts from the active nuclei at the centers of the dominant group galaxies, possibly triggered by merger activity (see, e.g. David et al. 2009 for a study of the NGC 5044 group). The dynamical processes in these scenarios may act individually

<sup>3</sup> <http://www.cfa.harvard.edu/~huchra/zcat/>.

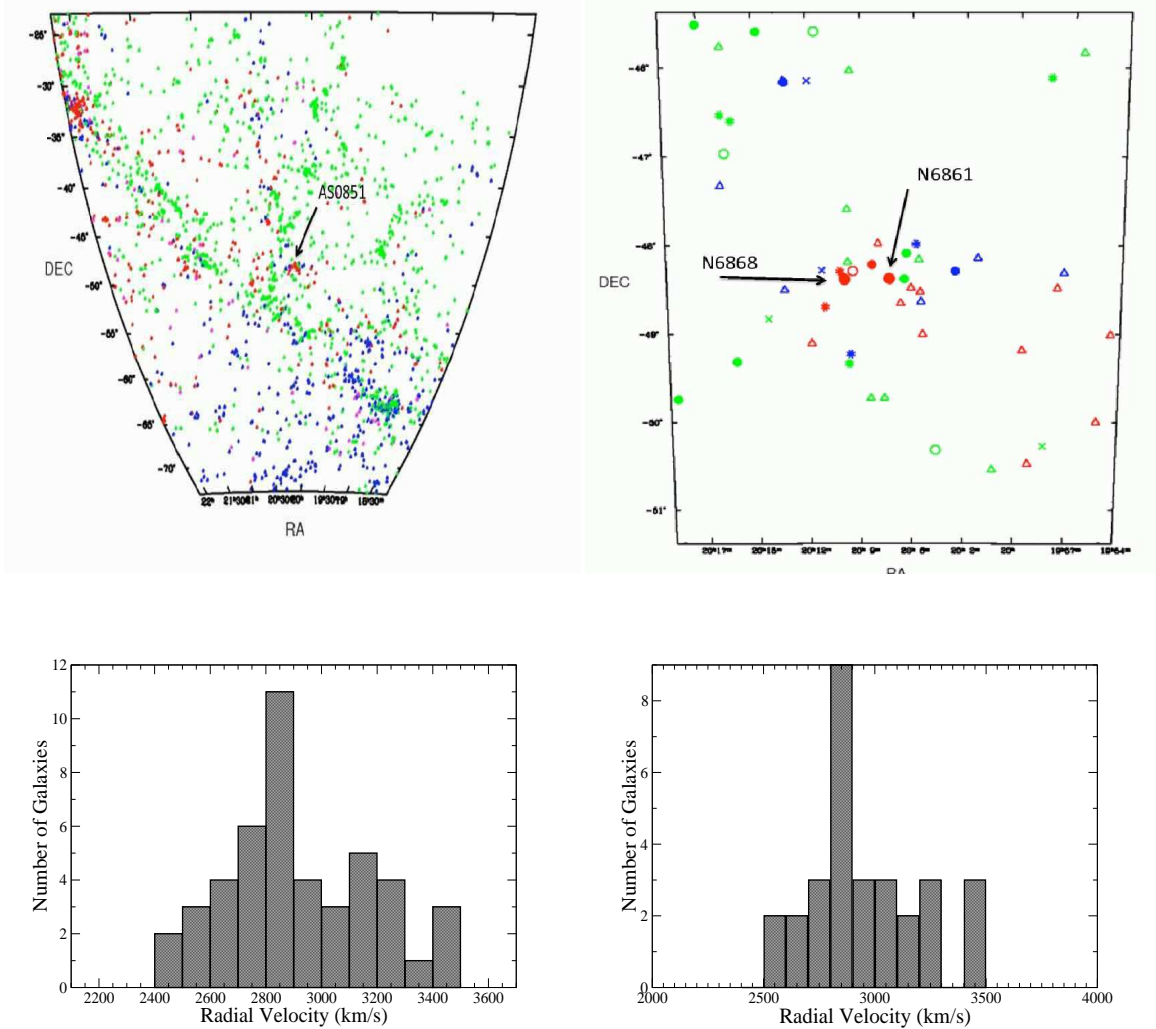


FIG. 5.— (*upper left*) Large scale structure environment of the Telescopium (AS0851) group from the CfA Redshift Survey 2008. Colors denote radial velocity bins of  $< 1500 \text{ km s}^{-1}$  (magenta),  $1500 - 2999 \text{ km s}^{-1}$  (red),  $3000 - 4499 \text{ km s}^{-1}$  (blue),  $4500 - 5999 \text{ km s}^{-1}$  (green). The arrow denotes the position of the AS0851 galaxy group. Shapes indicate galaxy morphology based on T type: solid circles (ellipticals,  $T = -7$  to  $-3$ ); open circle (spheroidals,  $T = -2$  to  $0$ ); asterisk (early type spirals Sa-c,  $T = 1$  to  $5$ ); crosses (late type spirals and irregulars Sd - Im,  $T = 6$  to  $10$ ); triangles (unclassified) and increasing symbol size denotes decreasing magnitude. Coordinates are J2000.0. (*upper right*) Galaxy distribution within  $2^\circ$  of the brightest group galaxy NGC 6868 with the same symbols as in the upper left panel. (*lower left*) Radial velocity histogram of all galaxies with radial velocities  $2000 < v_r < 4000 \text{ km s}^{-1}$  within  $4^\circ$  (2 Mpc) of NGC 6868. (*lower right*) Radial velocity histogram of all galaxies with radial velocities  $2000 < v_r < 4000 \text{ km s}^{-1}$  within a 1 Mpc (124') radius of NGC 6868.

or together to effect the transformation of these galaxies and their environment.

#### 4.1. NGC 6868's Edge and Tail: the Case for Infall

##### 4.1.1. Modeling the Edge

The sharp X-ray surface brightness edge to the north of NGC 6868 and trailing tail to the south (see Fig. 2), suggest that NGC 6868 may be moving with respect to the group IGM. In Figures 7 and 8 we investigate the northern edge-like feature. Following Vikhlinin et al. (2001), we construct the  $0.5 - 2 \text{ keV}$  surface brightness profile for NGC 6868 across the edge using elliptical annuli, centered on NGC 6868's nucleus and constrained to lie in an angular sector extending from  $41.5^\circ$  to  $164.5^\circ$ , to avoid the northwestern cavity. The elliptical annuli are chosen concentric to a bounding ellipse that traces the surface brightness discontinuity in the sector of interest (see Fig. 7). The width of each elliptical annulus

increases (decreases) with constant logarithmic step size as one moves outward (inward) from the bounding ellipse. Beyond 50 kpc, the elliptical annuli are no longer fully contained within the ACIS-I field-of-view. We define three narrow rectangular regions (also shown in Fig. 7) to extend the surface brightness profile to larger radii.

The resulting profile is shown in Figure 8. In the upper panel of Figure 8 we compare the surface brightness profile across the northern edge (filled squares) to the azimuthally averaged profile for the galaxy (open circles). We see a sharp, statistically significant, drop in surface brightness between  $20 \lesssim r \lesssim 35 \text{ kpc}$ , consistent with the presence of an edge. To model the X-ray surface brightness profile across the edge, we integrate the square of the electron density  $n_e$  times the corresponding X-ray emissivity  $\Lambda$  along the line of sight, assuming that the electron density on either side of the discontinuity is

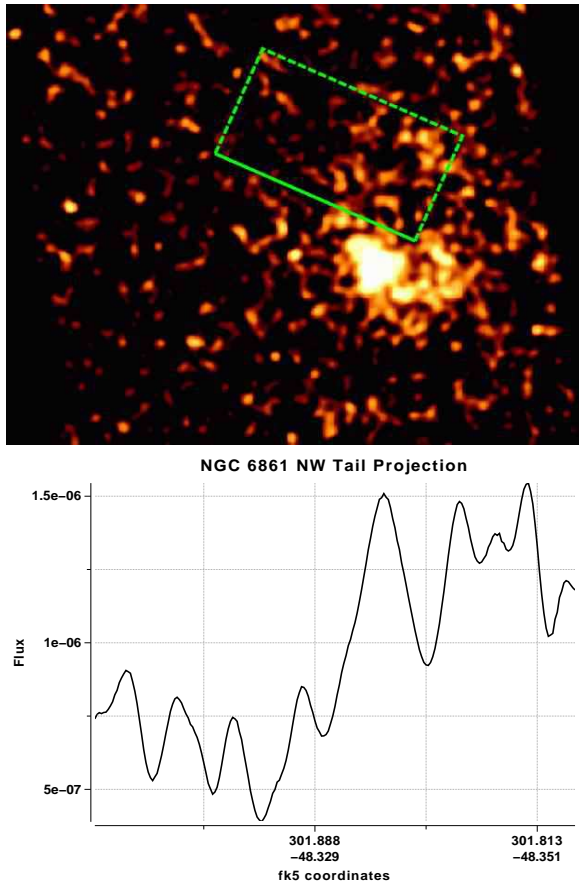


FIG. 6.— (upper) Background subtracted, exposure corrected 0.5–2 keV *Chandra* X-ray image of NGC 6861 showing a plume of emission to northeast, a bright tail to the west, and a fainter tail-like feature extending to the northwest. The image has been smoothed with an 8'' gaussian kernel. (lower) Projection of surface brightness in the rectangular region in the upper panel, showing a factor  $\sim 2$  enhancement in surface brightness in the northwestern tail over that in the adjacent IGM.

well described by spherical power law models of the form:

$$\begin{aligned} n_e &= n_1 \left( \frac{r}{r_{\text{edge}}} \right)^{-\alpha_1}, & r < r_{\text{edge}} \\ n_e &= n_2 \left( \frac{r}{r_{\text{edge}}} \right)^{-\alpha_2}, & r \geq r_{\text{edge}} \end{aligned} \quad (3)$$

where  $r_{\text{edge}}$  is the location of the edge. The observed surface brightness discontinuity is then given by

$$J^2 = \left( \frac{\Lambda_1 n_1^2}{\Lambda_2 n_2^2} \right), \quad (4)$$

where  $\Lambda_i$  and  $n_i$  are the X-ray emissivity and electron density for gas inside ( $i = 1$ ) and outside ( $i = 2$ ) the edge. We fit the surface brightness profile across the edge using a multi-variate chi-square minimization scheme allowing the edge position  $r_{\text{edge}}$ , electron density power law index  $\alpha_1$  inside the edge, and the size of the discontinuity (jump)  $J$  to vary. Since the signal-to-noise drops below 1 just outside the edge (see Fig. 8), the powerlaw index  $\alpha_2$  for the IGM gas density is not well determined by these data. We fix  $\alpha_2 = -1.56$  from the parameterization of the mean surface profile at large radii. The results of our model fits are listed in Table 2 and plotted in the lower panel of Figure 8, where we have varied the fit range

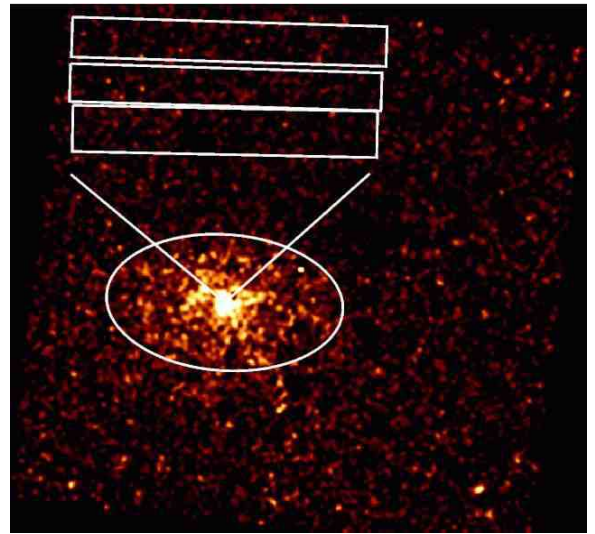


FIG. 7.— 0.5–2 keV blank-sky background subtracted, exposure corrected *Chandra* image of NGC 6868 with the angular sector ( $41.5^\circ$  to  $164.5^\circ$ ), bounding ellipse centered on NGC 6868's nucleus with (major, minor) axes and position angle of ( $228''3$ ,  $131''9$ ) and  $96^\circ$ , respectively. Outer box regions, used to construct the surface brightness profile at large radii, are superposed.

to probe the sensitivity of the edge position and jump discontinuity to the low S/N data. We find  $r_{\text{edge}} \sim 23 \pm 3$  kpc and jump discontinuity  $J \sim 2.2^{+0.4}_{-0.5}$ .

To complete the density model, we compute the X-ray emissivity  $\Lambda$  in the 0.5–2 keV energy band from APEC thermal plasma models for the X-ray emission from elliptical annular sectors, listed in Table 3, chosen concentric to the edge bounding ellipse (see Fig. 7) inside (NEdge<sub>-1</sub>) and outside (NEdge<sub>+0</sub>, NEdge<sub>+1</sub>) the edge. The results of these spectral fits are given in Table 4. Although the uncertainties are large, the temperature of the IGM outside the edge to the north is higher ( $0.73^{+0.07}_{-0.09}$  keV) than inside the edge ( $\sim 0.64 \pm 0.08$  keV), suggesting that the edge is a cold front. For temperatures  $\lesssim 1$  keV, the Fe L complex line emission dominates the thermal continuum in the 0.5–2 keV energy band, such that the X-ray emissivity depends sensitively on the abundance of the gas, and can vary by a factor  $\sim 5$  as the abundance varies from 0.1 to  $1Z_\odot$ . This introduces an uncertainty in the inferred density ratio across the edge by a factor  $\sim 2$ . Although the abundances are poorly constrained by these data, the spectral models in Table 4 suggest that low abundances ( $A \lesssim 0.3Z_\odot$ ) are favored in the group IGM north of the edge, consistent with abundances measured in other cool groups and in the outskirts of clusters (Rasmussen & Ponman 2007; Finoguenov et al. 2000; De Grandi et al. 2004). The spectral models in Table 4 also suggest that higher abundances  $A \sim 0.5 - 1Z_\odot$  are favored inside the edge closer to the center of NGC 6868, consistent with abundances measured in other dominant elliptical galaxies (see, e.g. Finoguenov & Jones 2001; Matsushita et al. 2003).

For simplicity we define a pair of fiducial spectral models with temperature  $kT = 0.73$  keV and abundance  $A = 0.3Z_\odot$  for IGM gas to the north, outside the edge, and  $kT = 0.64$  keV and  $A = 0.5Z_\odot$  for galaxy gas inside the edge. Normalizing the density model using the IGM gas density from eq. 3 at  $r = 34$  kpc to the north, where the contribution from the galaxy gas is negligible (see Fig. 3), we find an electron density in

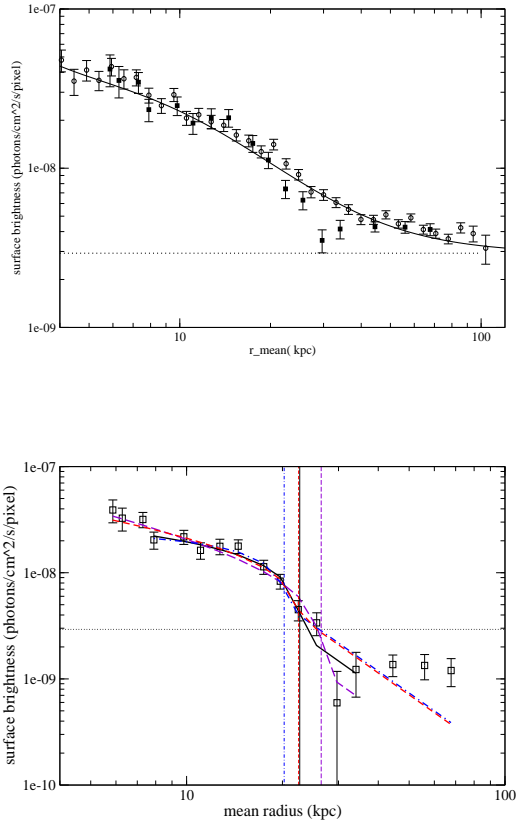


FIG. 8.— (*upper*) 0.5–2 keV surface brightness profile across the northern edge of NGC 6868 (filled squares), using the regions shown in 7, superposed on the azimuthally averaged 0.5–2 keV surface brightness profile from the upper panel of 3 (open circles). The lines are defined as in Fig. 3. (*lower*) Model fits to the northern surface brightness edge in NGC 6868 in the sector shown in Fig. 7. Open squares denote the surface brightness profile after subtraction of the soft Galactic background. Curved lines denote the density model fits to the background-subtracted surface brightness profile across the edge over the radius range 7.9–34 kpc (solid black), 7.9–68 kpc (dot-dash blue), 5.8–35 kpc (long dash violet), and 5.8–68 kpc (short dash red) listed in Table 2. The corresponding vertical lines denote the edge position in each case and the dotted horizontal line shows where  $S/N = 1$ .

the IGM  $n_e(r = 34 \text{ kpc}) = 4.4 \times 10^{-4} \text{ cm}^{-3}$ . Combining this with the density model fits to the edge location and surface brightness jump from eq. 4, we find electron gas densities at  $r = r_{\text{edge}}$  inside ( $n_1$ ) and outside ( $n_2$ ) NGC 6868’s northern surface brightness edge to be  $(1.2–1.5) \times 10^{-3} \text{ cm}^{-3}$  and  $(0.66–1.0) \times 10^{-3} \text{ cm}^{-3}$ , respectively (see Table 2). Note that if there is no abundance gradient across the edge, the density ratio derived from eq. 4 would be 23% larger.

#### 4.1.2. Velocity Constraints

To constrain the relative motion of NGC 6868 with respect to the ambient IGM, we assume uniform gas flow past a rigid spheroid, such that the difference between the gas pressure in the undisturbed IGM (free stream region) and that at the stagnation point of the flow, where the relative velocity of the IGM gas and galaxy gas vanishes, is the ram pressure due to the motion of the galaxy through the IGM (Vikhlinin et al. 2001). The pressure ratio  $p_0/p_2$  between IGM gas at the stagnation point and that in the free-stream region allows us to deter-

mine the Mach number of the flow (Landau & Lifshitz 1959) and thus the three-dimensional velocity of the infalling galaxy with respect to the ambient gas. Since the stagnation region is small and difficult to observe, and pressure is continuous across a cold front edge, we use the pressure in NGC 6868 just inside the northern edge ( $p_1$ ) as a proxy for the pressure at the stagnation point. We use the density and spectral model fits to gas inside and outside NGC 6868’s northern edge, given in Tables 2 and 4, to compute the range of pressure ratios ( $p_1/p_2$ ) and Mach numbers consistent with the fits to the surface brightness discontinuity (see Fig. 8). Our results are given in Table 5.

For all models, the inferred velocity for NGC 6868 relative to the surrounding group gas is at most transonic, i.e.  $v \leq 475 \text{ km s}^{-1}$  (Mach  $\leq 1.08$ ), given the speed of sound  $c_s = 440_{-30}^{+20} \text{ km s}^{-1}$  for 0.7 keV group gas. This is similar to that found in other infalling galaxies, such as NGC 1404 in Fornax (Machacek et al. 2005a) and, if we assume NGC 6861 rather than NGC 6868 is at the group center, not unexpected given the  $\sim 200 \text{ kpc}$  ( $\sim 0.3r_{500}$ ) separation between the two galaxies. On the other hand, the uncertainties in the observed metal abundances are large, and, since the spectrum for cool ( $\lesssim 1 \text{ keV}$ ) gas is dominated by the Fe L complex line emission, the emissivity of X-ray gas is highly dependent on the metal abundance of the gas. Solar abundances are often measured in the centers of dominant elliptical galaxies in groups (for a compilation, see, e.g. Rasmussen & Ponman 2007 and references therein). If we assume that solar abundances extend all the way to the surface brightness discontinuity in NGC 6868, the sharp jump in surface brightness may be explained by the ratio of abundances (and thus emissivities) across the edge alone. In that case, NGC 6868 may be at rest with respect to the surrounding IGM and likely at the center of the group potential. However, then stripping could not explain the origin of the southern tail.

#### 4.1.3. NGC 6868’s Southern Tail

As suggested in Figure 2 and confirmed in the lower panel of Figure 11, X-ray emission (and thus gas density) is higher to the south of the galaxy ( $171.5^\circ < \phi < 351.5^\circ$ ) than to the north at the same radii. If the southern tail is composed of ram-pressure stripped galaxy gas, we would expect the metal abundance in the southern tail to be higher, similar to abundances inside the edge in the galaxy gas halo, than in the IGM to the north. To test whether the southern tail is gas ram-pressure stripped from NGC 6868, we fit the spectrum from an elliptical annular sector ( $S_{+1}$ ) at the same mean radial distance and with the same radial bin width as sector NEdge $_{+1}$  to the north (see Table 3), but constrained to lie in the tail to the south between  $213^\circ$  to  $327.5^\circ$ . As shown in Table 4, the best fit single APEC model for this southern region gives a gas temperature and abundance of  $0.63_{-0.06}^{+0.05} \text{ keV}$  and  $0.29_{-0.18}^{+0.24} Z_\odot$ , respectively. While the temperature of the gas in this region is lower than that of the IGM to the north and comparable to the temperature of galaxy gas within NGC 6868, as one might expect if the gas were ram-pressure stripped galaxy gas, the uncertainties in the measured abundance are too large to definitively determine the origin of gas in the southern tail. Deeper X-ray data are needed to distinguish between: (1) cool, higher abundance ( $\sim 0.5 Z_\odot$ ) ram-pressure stripped galaxy gas, (2) lower temperature, lower entropy subgroup gas with an abundance comparable to that found in the IGM to the north, or (3) a multiphase mixture of the two, possibly signaled by the low



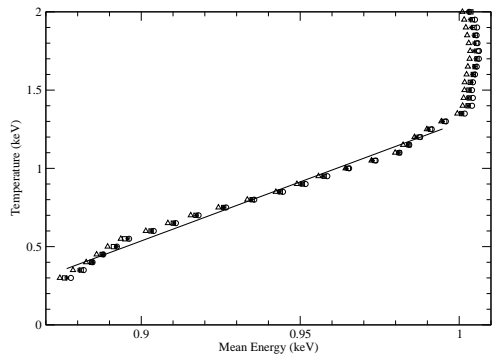


FIG. 9.— Gas Temperature as a function of mean photon energy in the 0.7–1.2 keV energy band for ACIS-I CCD I0 (circles), I1 (squares), I2 (triangles), and I3 (asterisks), assuming a single temperature APEC model with fixed metal abundance  $A = 0.5Z_{\odot}$  and Galactic absorption of  $3.9 \times 10^{20} \text{ cm}^{-2}$ . The solid line denotes the best linear fit ( $kT = -6.258 + 7.5492E$ ) restricted to  $0.4 \leq kT \leq 1.3$  keV.

90% CL lower bound on the abundance ( $\sim 0.11 Z_{\odot}$ ) from the single temperature APEC model fit (Buote 2000).

#### 4.2. Temperature Asymmetries: the Case for Sloshing

Modest density jumps and subsonic relative velocities, as observed for NGC 6868, are also characteristic of gas ‘sloshing’, where the surrounding IGM has been set in motion by the gravitational perturbation of a prior passage of galaxies or galaxy subgroups past each other in the group core (Markevitch et al. 2001). Simulations of sloshing in subcluster mergers show that the signatures of sloshing are most pronounced in the temperature structure of the gas, often producing cool, spiral-shaped tail-like features, as higher entropy gas from larger radii is mixed with the nearby lower entropy galaxy and subgroup gas (Ascasibar & Markevitch 2006).

##### 4.2.1. Temperature Map

Since NGC 6868 and NGC 6861 are elliptical galaxies in only a moderately massive galaxy group, we expect temperatures for gas in the galaxies and surrounding group/subgroup gas to be  $\lesssim 1$  keV. For such low gas temperatures the X-ray spectrum peaks at  $\sim 1$  keV and is dominated by lines in the Fe L complex. Using XSpec simulations of single temperature APEC plasma models, we find that there is nearly a linear correspondence between the temperature of the X-ray emitting gas in the 0.4–1.3 keV range and the mean photon energy measured in the 0.7–1.2 keV energy band, containing the Fe L emission (See Fig. 9 and David et al. 2009). We exploit this correspondence to construct the temperature map of NGC 6868 and NGC 6861, shown in Figure 10. After resolved point sources have been removed, we adaptively smooth the narrow (0.7–1.2 keV) band *Chandra* surface brightness images for NGC 6868 and NGC 6861 to determine regions of interest. We then average the photon energy in the Fe L peak over these regions and use the calibration shown in Figure 9 to relate these mean energies to the gas temperature. To check that our results were not an artifact of the binning procedure, we constructed a second temperature map, shown in the lower left panel of Figure 10, by explicitly fitting single temperature APEC models to regions containing

a minimum of 500 counts (O’Sullivan et al. 2005; Maughan et al. 2006; Randall et al. 2008). Although the second binning is much coarser and averages over the nuclear region in each galaxy, the results for the extended emission outside the nucleus are qualitatively the same.

The temperature maps confirm that the gas temperature in NGC 6868 inside (south of) the surface brightness edge is lower than in the group IGM to the north outside the edge. The lowest temperature gas ( $\sim 0.59$  keV) in NGC 6868 is displaced  $\sim 10$ – $20$  kpc ( $1.2$ – $2.5$ ) to the east of NGC 6868’s nucleus. There is a ring of higher temperature gas close to the nucleus, possibly indicating nuclear activity. The extended gas tail to the south of NGC 6868 is cool ( $\sim 0.65$  keV), and appears to spiral to the south and southwest around a  $\sim 30$  kpc long finger of higher temperature emission southwest of the nucleus. Both temperature maps show the spiral feature in NGC 6868’s extended southern tail. Although the temperature of the southern tail is consistent with that expected for ram-pressure stripped galaxy gas and such tails may curve, following the orbit of the infalling galaxy or subgroup, the tightly wound spiral pattern of cool gas wrapping about a higher temperature filament is more characteristic of the ‘sloshing’ signatures seen in simulations of IGM gas set in motion by interactions of galaxies or subcluster cores near the centers of clusters (Tittley & Henriksen 2005; Ascasibar & Markevitch 2006). Such features have been observed recently in X-ray observations of sub-cluster mergers and in galaxy groups (e.g see Markevitch & Vikhlinin 2007 for A2142; Mazzotta & Giacintucci 2008 for MS1455.0+2232; Johnson et al. 2009 for A1644; Randall et al. 2009 for the NGC 5098 group).

The temperature structure of NGC 6861 is dramatically different. In both temperature maps, single temperature APEC models suggest that the temperature of gas in the bright western tail is higher than in the surrounding IGM. Such high temperature tails have been observed in other galaxy groups, but are rare (see, e.g. Osmond et al. 2004 for the NGC 5171 group; Machacek et al. 2005b for the Pavo group). The upper panels of Figure 10 also show a sheath of high temperature gas  $\sim 8$  kpc ( $1'$ ) from NGC 6861’s center, well outside the X-ray bright central region of NGC 6861. There is no feature in the temperature maps corresponding to the northwestern tail observed in the X-ray surface brightness images (Figure 6).

##### 4.2.2. Spectral Modeling

We extracted spectra from regions based on the temperature map features for detailed fitting using XSpec 11.3.0. These regions are overlaid on the temperature and surface brightness maps in the upper right and lower right panels of Figure 10, respectively, and are listed in Table 6 for NGC 6868 and Table 8 for NGC 6861. The data were binned to ensure a minimum of 20 counts per bin and also using constant logarithmic bin size. We found no significance differences in the results obtained from these two binning methods. Backgrounds were taken from rescaled blank sky background sets (see §2), extracted from the same region as each source. We model the spectra using absorbed APEC thermal plasma (Smith et al. 2001) or APEC plus power law models and fit the data over the 0.5–7 keV energy range. To check our sensitivity to the soft Galactic background, we refit the data over the 0.7–7 keV range where this soft Galactic background will not contribute and found the fits unchanged.

##### NGC 6868:

For NGC 6868 we concentrate on features in and to the

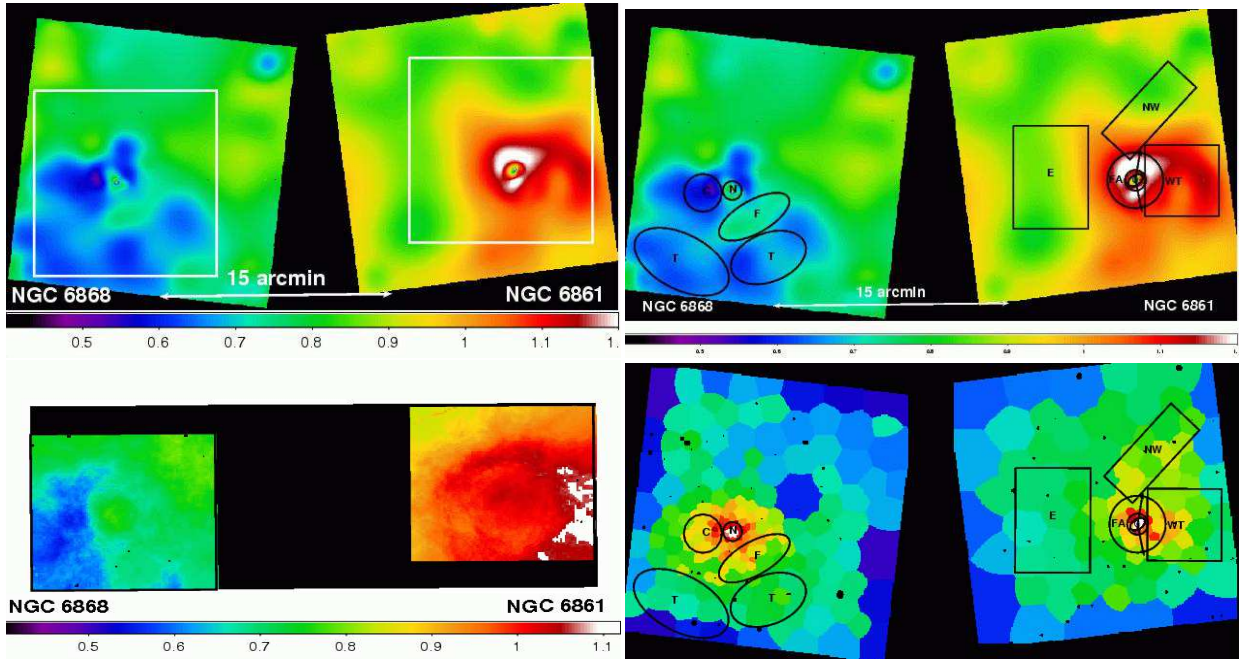


FIG. 10.— (*upper left*) Temperature map of NGC 6868 and NGC 6861 constructed from the mean photon energy in the Fe peak at 0.7–1.2 keV. Rectangular regions correspond to fields fit with the coarse temperature map shown below in the lower left panel (*upper right*) Same temperature map with spectral regions from Tables 6 and 8 superposed. N and G mark the centers of NGC 6868 and NGC 6861, respectively. (*lower left*) Coarse temperature map constructed by explicitly fitting single temperature APEC models to regions containing a minimum of 500 counts. (*lower right*) Spectral regions from Tables 6 and 8 on the adaptively binned 0.5–2 keV Chandra X-ray image of NGC 6868 and NGC 6861 from Fig. 2.

south of the galaxy. We extract spectra for the nuclear region of the galaxy (N), the lowest temperature region east of NGC 6868’s center (cold clump C), the filament of higher temperature gas to the southwest (F) and the lower temperature, spiral tail-like feature (the combined regions T). The results of our spectral fits for NGC 6868, listed in Table 7, generally confirm the results of Figure 10. The galaxy nucleus is well described by a two component APEC + power law model with gas temperature  $0.63^{+0.07}_{-0.06}$  keV, solar abundance, and power law index  $\sim 1.4$  to account for unresolved X-ray binaries in the central region of the elliptical galaxy and/or a weak AGN. Outside NGC 6868’s central region, the spectrum of the higher temperature filament (region F) and the southern spiral-like tail (region T) are both well described by single APEC thermal plasma models with temperatures of  $0.70 \pm 0.05$  and  $0.62 \pm 0.04$  keV, respectively. APEC models for the filament F have a modestly improved reduced  $\chi^2$  for low abundances ( $\sim 0.3-0.2Z_{\odot}$ ), suggesting that the filament may be composed of IGM rather than galaxy gas. The most problematical region to interpret in the temperature map of NGC 6868 is the cool clump region C. While a statistically acceptable fit (null = 0.09) is found for a single temperature ( $kT = 0.59^{+0.04}_{-0.05}$  keV) APEC model, there are significant residuals in the 0.7–1 keV region and the  $\chi^2/\text{dof} = 38/28$  is not particularly good. Addition of a second APEC or power law component did not improve the fit.

#### NGC 6861:

To determine the thermodynamics properties of gas surrounding the spheroidal galaxy NGC 6861, we measure the gas temperature in three rectangular regions: region E located 43.2 kpc to the east of NGC 6861’s nucleus in the direction of NGC 6868, region NW located to the northwest coincident with the northwestern tail shown in Figure 6 and

in the lower right panel of Fig. 10, and region WT containing the bright tail to the west of NGC 6861. We also model spectra within NGC 6861 using an elliptical region G centered on NGC 6861’s nucleus with semi-major (minor) axes of 4.2 (2.6) kpc, respectively, containing the nucleus and brightest galactic emission (see Fig. 4), and in a forward annular sector FA, with inner and outer radii of 5.3 kpc and 14.3 kpc, respectively, and constrained to lie between  $80^{\circ}$  and  $282^{\circ}$  measured counter-clockwise from west, containing the plume (Fig. 6) and ‘sheath’, identified in Figure 10, surrounding the galaxy’s central region. The results of our spectral fits to these regions are listed in Table 9. The central region of the galaxy (G) is well modeled by a  $0.66^{+0.11}_{-0.07}$  keV APEC model, describing the contribution of the diffuse galaxy gas, plus a power law component with photon index  $1.86 \pm 0.6$ , consistent with an active nucleus or population of unresolved X-ray binaries. The temperature of gas in the forward annulus region (FA) is significantly higher ( $1.27 \pm 0.15$  keV), in agreement with Figure 10, and higher metal abundances ( $\gtrsim 0.5Z_{\odot}$ ) are favored, as expected for gas associated with the galaxy. Gas in the western tail is well described by a single temperature APEC model, with gas temperature  $kT = 1.18^{+0.10}_{-0.12}$  and abundance  $0.25^{+0.21}_{-0.13}Z_{\odot}$ , confirming that the temperature in the western tail (WT) is also high. The low best fit metallicity in region WT, albeit with large uncertainties, favors a large IGM component rather than a purely galaxy origin for the gas in the western tail.

The properties of the X-ray emission to the northwest and east of NGC 6861 are more uncertain. The temperature and abundance of gas to the northwest of NGC 6861, along the possible northwestern tail, are  $0.90^{+0.09}_{-0.1}$  keV and  $0.22^{+0.26}_{-0.11}Z_{\odot}$ , with similar abundance but lower temperature than gas in the western tail. In contrast, a single temperature APEC model

fit to the spectrum in region E east of NGC 6861 (denoted fit E1 in Table 9) gives a low gas temperature ( $\sim 0.62^{+0.14}_{-0.11}$  keV), consistent at the 90% CL with the gas temperature to the north of NGC 6868. However, the best fit abundance is anomalously low ( $\lesssim 0.06Z_{\odot}$ ) in that model when compared to metallicities outside dominant galaxies in other galaxy groups, and the residuals show a ‘see-saw’ pattern often associated with multi-temperature gas (Buote 2000). A two-component APEC model (denoted E2 in Table 9) with a more realistic abundance value of  $0.2Z_{\odot}$ , consistent with the best fit abundances found in the northwest and western tail regions, yields gas temperatures of  $\sim 0.46^{+0.17}_{-0.13}$  keV and  $\sim 1.24^{+0.31}_{-0.17}$  keV, but the reduced  $\chi^2$  is unchanged over that for the single APEC fit. Deeper observations are required to disentangle the complex temperature structure to the east of NGC 6861.

#### 4.2.3. NGC 6861’s Tails: Stripping or Slushing?

Since bifurcated tails are common features in ram-pressure stripped galaxies, such as those infalling into the Virgo cluster (see, e.g. Randall et al. 2008), NGC 6861’s bright western and fainter northwestern tails might suggest that it is infalling towards NGC 6868 near the core of the AS0851 galaxy group. However, most ram-pressure stripped tails are composed of galaxy gas with higher metallicities and lower gas temperatures than the surrounding group IGM, in contradiction with the  $\gtrsim 1$  keV gas temperatures and low ( $\sim 0.2$ ) best-fit abundances measured in NGC 6861’s tails. Long, hot tails can be formed by turbulent-viscous stripping of galaxy gas and its subsequent mixing and thermalization with the group IGM during supersonic motion of the galaxy through the ambient group gas, or by gravitational focusing of the IGM into an adiabatically heated Bondi-Hoyle wake (see, e.g. Machacek et al. 2005b). However, when such supersonic infall occurs in the plane of the sky, as we expect here (see §3.3), we should see a rise in temperature and density along a narrow shock front preceding the motion, followed by a cold front edge closer to the galaxy. We do see higher temperature gas ( $kT \sim 1.3^{+0.3}_{-0.2}$  keV), compared to the ambient IGM ( $\sim 0.7 - 0.9$  keV), in the sheath surrounding NGC 6861 (region FA in Fig. 10). If the factor  $\sim 1.9$  temperature rise in the sheath is due to a shock, we would expect to see a corresponding factor  $\sim 2$  increase in density from the Rankine-Hugoniot conditions and, thus, a surface brightness increase by a factor 4 in the same region (see, e.g. Landau & Lifshitz 1959). Although we find no evidence in these data for the sharp change in surface brightness (and thus density) that would be associated with such a shock, nor do we see the associated merger cold front expected if NGC 6861 were moving supersonically in the plane of the sky through the ambient IGM, projection effects in these sparse data may make such features difficult to observe.

A more promising scenario may be that surface brightness and temperature asymmetries are the result of a gravitational encounter between NGC 6868 and NGC 6861, each the dominant galaxy in their own subgroup. Then the dark matter distribution is bimodal, with each galaxy residing near its own local minimum of the gravitational potential. This would explain why double  $\beta$ -models provide a good description of the mean surface brightness profile around each galaxy. However, since the merger is likely occurring in the plane of the sky, this subgroup structure may be difficult to discern from the optical galaxy distributions. We may be viewing the encounter after the subgroups have passed through pericenter, but be-

fore the gas halos have been completely stripped and merged. The strong temperature and surface brightness asymmetries around each of the merging partners may be due to non-hydrostatic motions of the gas (‘slushing’), as gas is displaced from the center of each subcluster’s dark matter potential, similar to those produced in simulations of premerger encounters of more massive subcluster halos. When gas is present in both halos, cold fronts with cool spiral-shaped tails may form about one subcluster, while higher temperature shock-heated features may form around the other (see Figure 9 of Ascibar & Markevitch 2006). These simulations suggest that the asymmetries persist for gigayears after the encounter. Thus the observation of slushing signatures around each galaxy, even though they are separated by 207 kpc (sound crossing time of 500 Myr), is reasonable.

#### 4.3. The Case for AGN Feedback

AGN activity and black hole growth may be influenced by either ram pressure, through backflow of partially stripped material onto the central regions of the galaxy, or during a close gravitational encounter between two galaxies, that would also produce slushing. Since both NGC 6868 and NGC 6861 currently host weak radio sources at their nuclei consistent with AGN, we look for signatures in the X-ray gas that might signal past episodes of more energetic AGN activity.

##### 4.3.1. ‘Ghost’ Cavities Near NGC 6868?

Figures 2 and 11 show a roughly circular deficit in X-ray surface brightness centered 4.9 (in projection) to the northwest of NGC 6868’s nucleus. In the upper panel of Figure 11 we use 8 annular sectors, centered on the nucleus of NGC 6868 and with inner and outer radii of  $168''$  (22.5 kpc) and  $387''$  (51.9 kpc), respectively, to investigate more quantitatively this northwest cavity. We denote the position of each sector by the mean angle  $\phi$  for the sector measured counter-clockwise from the  $+x$  axis (west). In the lower panel we plot the number of net source counts in each annular sector in the 0.5–2 keV energy band as a function of sector position. Error bars represent  $1\sigma$  uncertainties in the net source counts. We find that the number of net counts ( $187 \pm 19$ ) in the sector coincident with the northwest cavity ( $\phi = 37.5^\circ$ ) is lower by  $\gtrsim 3\sigma$  than the counts in its neighboring sectors, ( $281.3 \pm 21.4$  counts at  $\phi = 81.5^\circ$  and  $440.2 \pm 24.7$  counts at  $\phi = -8.5^\circ$  [ $351.5^\circ$ ]).

The cavity candidate is a ‘ghost’ cavity, since no radio emission has as yet been observed in this region, has low contrast and no well defined rim, similar to the radio-faint cavity in 2A 0335+096 (Birzan et al. 2004). Features of this kind need to be confirmed in deeper X-ray observations and explored with lower frequency radio observations to detect the radio plasma expected to reside in their interiors. Furthermore, the projected spherical morphology is somewhat puzzling given the evidence for gas motions in §4.1 and §4.2 that might distort the cavity’s shape. However, assuming the cavity is an evolved buoyant bubble filled with relativistic radio plasma from past AGN activity, we may use the geometry of the cavity and the mean pressure in the surrounding IGM to estimate the enthalpy ( $4pV$ ) carried in the bubble. We calculate the mean pressure of gas that was evacuated to form the bubble from the density model in eq. 3 and the temperature of the IGM given in Table 4. Assuming a spherical bubble of radius 11.7 kpc ( $87''$ ) oriented close to the plane of the sky, we find

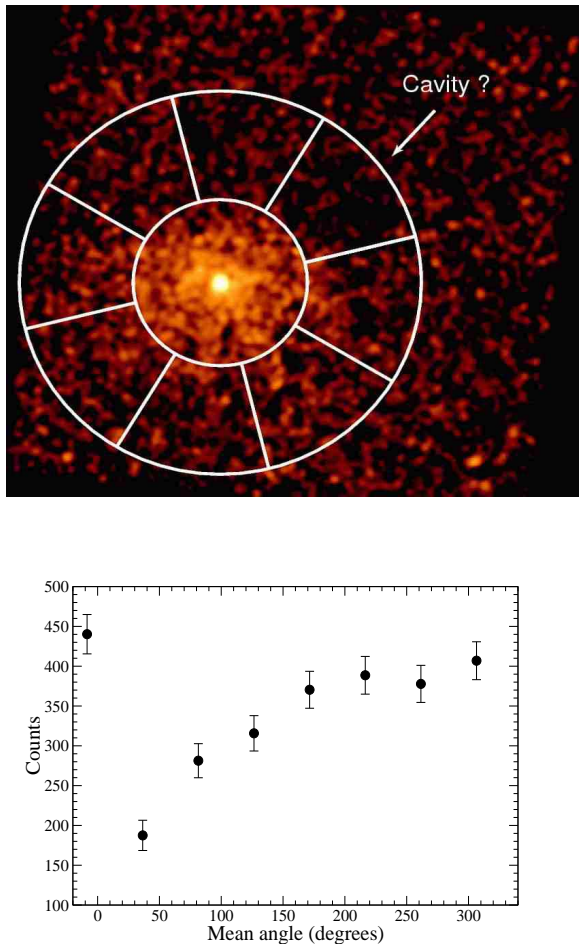


FIG. 11.— (*upper*) 0.5–2 keV blank-sky background subtracted, exposure corrected *Chandra* image of NGC 6868 with a panda region overlaid to identify X-ray surface brightness deficits (cavities) in the group IGM. 1 pixel =  $1''.968 \times 1''.968$  and the image has been smoothed with a  $6''$  Gaussian kernel. The annular sectors are centered on NGC 6868’s nucleus ( $20^{\text{h}}09^{\text{m}}54.1^{\text{s}}, -48^{\circ}22'46.4''$ ) with inner and outer radii of  $168''$  (22.5 kpc) and  $387''.6$  (51.9 kpc), respectively. North is up and east is to the left. (*lower*) Net source counts as a function of the mean angle  $\phi$  of the annular sector, measured counterclockwise from west. Error bars represent  $1\sigma$  uncertainties in the source counts. Note the surface brightness deficit at  $\phi = 36.5^{\circ}$ .

the enthalpy carried by the bubble of  $4pV \sim 5.9 \times 10^{56}$  ergs, similar to ghost cavities in Abell 262 (Blanton et al. 2004) or HCG 62 (Birzan et al. 2004) and to younger cavities in galaxies, such as M87 (Young et al. 2002; Forman et al. 2005) and NGC 4472 (Biller et al. 2004).

The age of the bubble may be estimated by assuming that (1) the bubble rises with the speed of sound  $c_s$  in the ambient medium  $t = d/c_s$ , (2) the bubble rises buoyantly at the terminal velocity  $v_t$  such that  $t = d/v_t \sim d\sqrt{SC/2gV}$ , where  $V$  is the volume of the bubble,  $S$  its cross-section, and  $C = 0.75$  the drag coefficient, or (3) the time  $t = 2\sqrt{r/g}$  for gas to refill the displaced volume as the bubble moves upward, where  $r$  is the radius of the cavity and  $g$  the acceleration of gravity (Churazov et al. 2001; McNamara et al. 2000; Nulsen et al. 2002; Birzan et al. 2004). For the northwestern bubble these imply bubble ages of 88, 107, 119 Myr, respectively, for the three methods, and a mechanical luminosity of  $L_{\text{mech}} \sim 1.8 \times 10^{41}$  erg s $^{-1}$ . Bubble ages of  $\sim 10^8$  yr are

typical for ghost bubbles in other systems (see, e.g. Birzan et al. 2004).

A partially rimmed, spherical X-ray surface brightness feature, with radius  $\sim 60''$  may also be seen in Figure 2 located  $3'.1$  to the southwest of NGC 6868’s nucleus. A filament of hot gas (region F in Fig. 10) is seen to cross the candidate cavity. If this feature is also a buoyant ghost bubble, perhaps broken by the hydrodynamic motions in the gas caused by interactions between NGC 6868 and NGC 6861, we estimate its enthalpy, age and mechanical power to be  $4 \times 10^{56}$  ergs, 55–78 Myr, and  $\sim 2 \times 10^{41}$  erg s $^{-1}$ , respectively, comparable to that of the northwest cavity.

#### 4.3.2. AGN Heating in NGC 6861?

The surface brightness in the plume rising to the northeast from NGC 6861 and in the western tail increase by factors  $\sim 2$  and  $\sim 3$ , compared to regions to the southeast at comparable distance from NGC 6861’s nucleus, and have a  $\sim 0.5$  keV higher temperature than the central region of that galaxy (see Fig. 10 and regions FA and WT compared to G in Table 9). One possible explanation is that gas in these regions may have been disturbed and heated by AGN activity. Assuming that the western tail is contained in a cylindrical volume oriented in the plane of the sky with radius 18 kpc and length 37.7 kpc (based on the WT spectral region), we find the tail contains  $\sim 2.6 \times 10^9 \eta^{1/2} M_{\odot}$  of hot gas. Since the gas in the tail appears clumpy, the filling factor  $\eta$  is likely less than one, so that this is an upper bound on the actual mass of hot gas in the tail. The energy necessary to raise the temperature of the gas in the tail from  $\sim 0.7$  keV found for gas in the bright central region of the galaxy (region G) or the surrounding IGM to 1.18 keV measured in the tail is  $\sim 6 \times 10^{57}$  ergs. Outburst energies of up to  $10^{61}$  ergs have been measured from shocks observed in, for example, Hercules A (Nulsen et al. 2005a) and Hydra A (Nulsen et al. 2005b), while outburst energies  $\sim 10^{58}$  ergs have been measured in M87 (Forman et al. 2005), whose  $3 \times 10^9 M_{\odot}$  central black hole has mass comparable to that inferred for NGC 6861 from the  $M_{\text{BH}} - \sigma_*$  relation. Thus energetic outbursts from a  $2.5 \times 10^9 M_{\odot}$  black hole at the center of NGC 6861 would have sufficient energy to heat and produce turbulent motions in the gas, that might also contribute to the disturbed gas morphology observed near NGC 6861.

## 5. ON NGC 6861’S BLACK HOLE MASS

The discrepancy between the black hole mass prediction from the Magorrian relation (eq. 2) and the  $M_{\text{BH}} - \sigma_*$  relation (eq. 1) is still difficult to understand. If NGC 6861’s black hole mass is large, then either an existing massive stellar bulge has been stripped from NGC 6861 or the coevolution of NGC 6861’s stellar bulge has been inhibited or delayed during a period of rapid black hole growth. In the first case, hydrodynamic processes such as ram pressure and turbulent viscous stripping, plasma outflows from AGN, or gas sloshing may heat and redistribute the gas in and around NGC 6861, but would be ineffective at changing the galaxy’s stellar distribution. Stars in the outer halo could be stripped tidally if the impact parameter of the collision between NGC 6861 with NGC 6868 is sufficiently small, as observed in dumbbell galaxy systems such as NGC 4782/NGC 4783. However, even in the deeply penetrating collisions of such dumbbell galaxies, simulations show that only 10–20% of the stellar mass is expected to be stripped (Madejsky & Bien 1993). For a  $2.5 \times 10^9 M_{\odot}$  black hole, equation 2 predicts a stellar bulge

mass for NGC 6861 of  $\sim 10^{12} M_{\odot}$ , such that previous interactions would have had to strip  $\sim 90\%$  of the stellar mass to be in agreement with the K-band mass estimates given in Table 1. One would expect to see evidence for such cataclysmic tidal disruption in tidal bridges, tails or other stellar morphological distortions, that are not observed in the stellar distributions of either NGC 6861 or NGC 6868. Also this scenario would imply the direct passage of the subgroup gas cores through each other and much more disruption in the X-ray gas in NGC 6868 than is observed.

The second case, in which the growth of the stellar bulge is inhibited, may be more likely. NGC 6861 shows evidence for a stellar bar (Koprolin & Zeilinger 2000). Stellar bars are likely to be formed in mergers and allow angular momentum of infalling matter to be dissipated. Gas and dust may then be transported along the bar to the galaxy's nuclear region to fuel one or several episodes of rapid black hole growth. If this accretion event triggers an AGN outburst in NGC 6861, gas otherwise available for star formation could be heated and inflated, delaying the expected growth of the bulge (Silk & Rees 1998). The total energy deposited into the ambient gas from an episode of rapid black hole growth is  $f\epsilon\Delta Mc^2$ , where  $\Delta Mc^2$  is the rest mass energy of the accreted matter,  $\epsilon$  is the fraction of the rest mass energy released in the accretion event, and  $f$ , the feedback efficiency, measures how efficiently that energy is coupled to the surrounding galaxy and subgroup gas. For the standard assumption of radiative efficient accretion ( $\epsilon = 0.1$ ) and efficient feedback  $f \gtrsim 0.05$  (Di Matteo et al. 2008; Churazov et al. 2002), the total energy deposited in the surrounding gas as the black hole grows from  $2.1 \times 10^8 M_{\odot}$  predicted by the Margorrian relation to  $2.5 \times 10^9 M_{\odot}$ , consistent with the  $M_{\text{BH}} - \sigma_*$  relation, would be large ( $\gtrsim 2 \times 10^{61}$  ergs). This is comparable to the most energetic AGN outbursts observed in massive clusters (see, e.g. Nulsen et al. 2005a for Hercules A; McNamara et al. 2002 for MS 0735.6+7421; Nulsen et al. 2005b for Hydra A). If accretion proceeds at the Eddington rate,

$$\dot{M}_{\text{Edd}} = (0.22/\epsilon)(M_{\text{BH}}/10^8)M_{\odot} \text{ yr}^{-1}, \quad (5)$$

the accretion timescale would be  $\sim 110$  Myr and the mean radiative power,  $\sim 10^{47} \text{ erg s}^{-1}$ . The power that couples to the surrounding gas ( $\sim 5 \times 10^{45} \text{ erg s}^{-1}$ ) is more than three orders of magnitude larger than that needed to balance X-ray cooling in the galaxy. Such an event would likely completely disrupt the gas in NGC 6861 and its subgroup. However the accretion and feedback efficiencies are highly uncertain. If the growth of NGC 6861's black hole was triggered by the ongoing merger with the NGC 6868 subgroup in AS0851, either the accretion is radiatively inefficient ( $\epsilon \ll 0.1$ ), the released rest-mass energy is only weakly coupled to the galaxy and subgroup gas ( $f \ll 0.05$ ; see, e.g., Kurosawa et al. 2009), and/or the black hole grows through multiple, less energetic outburst events over a much longer timescale. For example, if  $f\epsilon \sim 10^{-6}$ , the energy from AGN activity deposited in the surrounding subgroup gas from this episode of rapid black hole growth would be  $\sim 10^{58}$  ergs, sufficient to heat the western tail. Alternatively, the period of rapid black hole growth may have occurred at very early times, before NGC 6861 was assembled into the current galaxy group/subgroup structures in AS0851. Then a very strong AGN outburst, as indicated above, may have swept gas from the galaxy, delaying bulge formation by quenching star formation and heating or blowing

away any surrounding subgroup gas. Growth of the associated stellar bulge for NGC 6861 may only now be occurring, not through star formation, but by the cannibalization of the stellar distributions already in place as NGC 6861 merges with nearby galaxies in the group and ultimately NGC 6868 (Silk & Rees 1998).

A third possibility is that the Magorrian relation holds and the central black hole in NGC 6861 is  $\sim 2 \times 10^8 M_{\odot}$ , typical for early type galaxies in groups. Then gravitational interactions between NGC 6861 and NGC 6868 or other group galaxies would also need to increase the central stellar velocity dispersion in NGC 6861 to anomalously high values. Strong tidal forces in a deeply penetrating encounter may distort stellar velocity profiles, causing them to increase with distance from the galaxy center (see, e.g. Madejsky & Bien 1993 for NGC 4782). For finite apertures, this might contaminate the measurement of the central stellar velocity dispersion and thus cause the black hole mass to be overestimated. For example, the measurement of  $382 \pm 7 \text{ km s}^{-1}$  by Koprolin & Zeilinger (2000) is the average stellar velocity dispersion within  $5''$  (670 pc) of the galactic center, well outside the sphere of influence of the supermassive black hole. However, if the velocity dispersion profile has been affected by tidal forces in a merger, as in NGC 4782, one would expect that the stellar velocity dispersion would increase when averaged over larger radii, which is not observed in NGC 6861 (Koprolin & Zeilinger 2000). It is also difficult to understand in this scenario why the stellar velocity dispersion of NGC 6861 would be so profoundly affected by the interaction, while that of its likely interacting partner NGC 6868 is not. If the Magorrian relation holds, the anomalously high stellar velocity dispersion in NGC 6861 may require NGC 6861 to have experienced one or more recent minor mergers unrelated to the interaction with NGC 6868 that is responsible for the large scale gas sloshing observed in the group.

## 6. CONCLUSIONS

In this paper we used *Chandra* observations of NGC 6868 and NGC 6861 in the AS0851 galaxy group to measure the density and temperature structure of gas in these two dominant group elliptical galaxies. This system is particularly important because, although the brightest group galaxy has a black hole mass  $M_{\text{BH}} \sim 3.3 \times 10^8 M_{\odot}$  predicted by the  $M_{\text{BH}} - \sigma_*$  relation, that is both consistent with the Margorrian  $M_{\text{BH}} - M_{\text{bulge}}$  relation and typical of black hole masses inferred for the dominant galaxies in other cool groups, the central black hole mass inferred from the  $M_{\text{BH}} - \sigma_*$  relation for the second brightest group galaxy NGC 6861 ( $M_{\text{BH}} \sim 2.5 \times 10^9 M_{\odot}$ ) is more than an order of magnitude higher than that predicted by the Magorrian relation. The goal of this work was to use these X-ray data to explore possible interaction scenarios (infall and gas stripping, gas sloshing, AGN outburst activity) that might affect galaxy evolution and black hole growth.

We find:

- The X-ray surface brightness distributions around NGC 6868 and NGC 6861 are each well described by double  $\beta$ -models with inner (outer) beta and core radii of 0.65 and 0.49 kpc (0.52 and 11 kpc) for NGC 6868 and 0.61 and 0.5 kpc (0.38 and 11.9 kpc) for NGC 6861. This suggests that NGC 6868 and NGC 6861 may each be the dominant galaxy in a galaxy subgroup that is merging. Lack of evidence for

substructure in the galaxy redshift distribution suggests that we would be viewing such a subgroup merger close to the plane of the sky.

- X-ray surface brightness and temperature maps of NGC 6868 show a cold front  $23 \pm 3$  kpc to the north of the galaxy nucleus and a spiral-shaped tail of cool 0.62 keV gas to the south, suggesting relative motion between the galaxy and the surrounding IGM. Analysis of the density and temperature across the edge constrains the relative motion between NGC 6868 and the IGM to be at most transonic ( $\lesssim 460 \text{ km s}^{-1}$ ). While we cannot rule out the possibility that the tail is composed of ram-pressure stripped galaxy gas, the tightly wound spiral-like morphology of the tail in the temperature map strongly suggests that the tail is a result of the ‘sloshing’ of gas in the gravitational potential, set in motion by the previous gravitational encounter between the NGC 6868 and NGC 6861 subgroups.
- X-ray surface brightness and temperature maps for NGC 6861, 206 kpc to the west of NGC 6868, show a complex morphology also suggestive of a subgroup merger. While spectra of the central  $\sim 5$  kpc of NGC 6861 containing the bright stellar disk is well described by a cool  $0.66^{+0.11}_{-0.07}$  keV thermal plasma model plus a power law with photon index  $-1.87$  for the central active galactic nucleus (AGN), the temperature of gas in the 5–14 kpc ‘sheath’ outside NGC 6861’s central region is a factor  $\sim 2$  higher. A hot (0.9–1.2 keV), bifurcated tail is seen trailing NGC 6861 38 kpc to the west and northwest. These features may suggest that the NGC 6861 subgroup is undergoing ram-pressure or turbulent-viscous stripping during supersonic infall towards NGC 6868. However, comparing the density and temperature morphologies of NGC 6868 and NGC 6861 taken together with simulations from the literature, the more likely explanation is that the hot features in NGC 6861 are the consequence of gas sloshing caused by the ongoing merger of two subgroups, whose

respective hot gas halos have not yet been stripped.

- NGC 6868 may have undergone a period of merger-induced AGN activity. X-ray surface brightness images show weak evidence for roughly circular surface brightness deficits to the northwest and southwest of NGC 6868. If confirmed in deeper X-ray images or low frequency radio observations to be buoyant bubbles filled with relativistic plasma from previous AGN activity, the bubbles’ enthalpies ( $5 \times 10^{56}$  ergs), mechanical power ( $2 \times 10^{41} \text{ erg s}^{-1}$ ) and ages ( $\sim 60\text{--}100$  Myr) are typical for ‘ghost’ cavities observed in other systems.

While the X-ray data favor a sloshing interaction scenario aided by AGN activity to explain possible cavities near NGC 6868 and gas heating in/near NGC 6861, an explanation for the discrepancy between the Magorrian and  $M_{\text{BH}} - \sigma_*$  relation predictions for the black hole mass at the center of NGC 6861 remains challenging. Deeper X-ray observations that probe closer to the central engine and map with greater precision the complex density and temperature structure of the gas are needed to constrain the gasdynamics and orbital parameters of the merger and determine the energies and timescales of associated AGN activity. More detailed theoretical modeling in gravity + hydrodynamic numerical simulations that are guided by those data may then be able to determine how mergers affect the high mass end of the black hole mass relations and solve the mystery of NGC 6861’s black hole mass.

This work is supported in part by NASA grant NNX07AH65G and the Smithsonian Institution. This work has made use of the NASA/IPAC Extragalactic Database (NED) which is operated by the Jet Propulsion Laboratory, California Institute of Technology, under contract with the National Aeronautics and Space Administration. We wish to thank John Huchra for help using the Harvard-Smithsonian CfA Redshift Survey (ZCAT) database for galaxy redshift data, Ryan Johnson and Paul Nulsen for helpful discussions, and an anonymous referee for helpful comments.

*Facilities:* CXO (ACIS-I)

#### REFERENCES

- Ascasibar, Y. & Markevitch, M. 2006, *ApJ*, 650, 102  
 Bautz, M.W., et al. 1998, *X-ray Optics, Instruments and Missions*, ed. R.B. Hoover & A.B. Walker. Proc. SPIE, 3444, 210  
 Beifiori, A., Sarzi, M., Corsini, E. M., Dalla Bonta, E., Pizzella, A., Coccato, L., Bertola, F. 2009, *ApJ*, 692, 856  
 Beuing, J., Döbereiner, S., Böhringer, H., & Bender, R. 1999, *MNRAS*, 302, 209  
 Biller, B.A., Jones, C., Forman, W.R., Kraft, R.P., & Ensslin, T. 2004, *ApJ*, 613, 238  
 Birzan, L., Rafferty, D. A., McNamara, B.R., Wise, M.W., & Nulsen, P.E.J. 2004, *ApJ*, 607, 800  
 Blanton, E.L., Sarazan, C.L., McNamara, B.R., & Clarke, T.E. 2004, *ApJ*, 612, 817  
 Bondi, H. 1952, *MNRAS*, 112, 195  
 Bondi, H. & Hoyle, F. 1944, *MNRAS*, 104, 273  
 Bregman, J. N., Snider, B. A., Grego, L., & Cox, C. V. 1998, *ApJ*, 499, 670  
 Buote, D. 2000, *MNRAS*, 311, 176  
 Buson, L. M., Sadler, E. M., Zeilinger, W. W., Bertin, G., Betola, F., Danzinger, J., Dejonge, H., Saglia, R.P., & de Zeeuw, P. T. 1993, *A & A*, 280, 409  
 Byrd, G. & Valtonen, M. 1990, *ApJ*, 350, 89  
 Cappellari, M., Verolme, E. K., van der Marel, R. P., Verdoes Kleijn, G. A., Illingworth, G. D., Franx, M., Carollo, C. M., & de Zeeuw, P. T. 2002, *ApJ*, 578, 787  
 Churazov, E., Brügggen, M., Kaiser, C.R., Böhringer, H. & Forman, W. 2001, *ApJ*, 554, 261  
 Churazov, E., Sunyaev, R., Forman, W. & Böhringer, H. 2002, *MNRAS*, 332, 729  
 Cooper, M. C. et al. 2006, *MNRAS*, 370, 198  
 David, L.P., Jones, C., Giacintucci, S., Forman, W.R., Nulsen, P., Vrtillek, J., O’Sullivan, E. & Raychaudhury, S. 2009, *ApJ*, in press, eprint arXiv:0905.0654  
 De Grandi, S., Ettori, S., Longhetti, M., Molendi, S., 2004, *A&A*, 419, 7  
 Di Matteo, T., Springel, V., Hernquist, L., & Sijacki, D. 2008, *ApJ*, 676, 33  
 Ellis, S. C. & O’Sullivan, E. 2006, *MNRAS*, 367, 627  
 Ferrarese, L. & Merritt, D. 2000, *ApJ*, 539, L9  
 Finoguenov, A. & Jones, C. 2001, *ApJ*, 547, L107  
 Finoguenov, A., David, L.P., Ponman, T.J. 2000, *ApJ*, 544, 188  
 Forman, W.R., Schwarz, J., Jones, C. Liller, W. & Fabian, A. 1979, *ApJ*, 239, L27  
 Forman, W., Nulsen, P., Heinz, S., Owen, F., Eilek, J., Vikhlinin, A., Markevitch, M., Kraft, R., Churazov, E., & Jones, C. 2005, *ApJ*, 635, 894  
 Fukazawa, Y., Botoya-Nonesa, J. G., Pu, J., Ohto, A. & Kawano, N. 2006, *ApJ*, 636, 698  
 Garmire, G.P. et al. 1992, AIAA, Space Programs and Technologies Conference, March 24-27, 1992 (Paper 92-1473; New York: AIAA)  
 Garcia, A. M. 1993, *A & AS*, 100, 47  
 Gebhardt, K., Bender, R., Bower, G., et al. 2000, *ApJ*, 539, L13  
 Gilfanov, M. 2004, *MNRAS*, 349, 146  
 Gunn, J. & Gott, J. 1972, *ApJ*, 176, 1  
 Hansen, L., Jorgensen, H. E., Norgaard-Nielsen, H. U. 1991, *A & A*, 243, 49  
 Hardcastle, M.J., Evans, D. & Croston, J.H. 2007, *MNRAS*, 376, 1849  
 Häring, N. & Rix, H.-W. 2004, *ApJ*, 604, L89  
 Hinshaw, G. et al. 2009, *ApJS*, in press, eprint arXiv:0803.0732v2  
 Johnson, R., Markevitch, M., Wegner, G., Jones, C. & Forman, W.R. 2009, *ApJ*, submitted

TABLE 1  
GALAXY PROPERTIES AND BLACK HOLE MASSES

Name	$K_s(\text{total})$	$M_*$ ( $10^{11}M_\odot$ )	$\sigma_*$ ( $\text{km s}^{-1}$ )	$M_{\text{BH}}^\sigma$ ( $10^8M_\odot$ )	$M_{\text{BH}}^*$ ( $10^8M_\odot$ )
NGC 6868	7.317	1.83	$250 \pm 10$	3.3	3.1
NGC 6861	7.708	1.28	$414 \pm 17$	25	2.1

NOTE. — Columns (1) galaxy name; (2) total 2MASS K-band luminosity (NED); (3) stellar mass (bulge mass) estimated using K-band luminosities (Gilfanov 2004); (4) stellar velocity dispersion (Wegner et al. 2003); (5) and (6) central black hole mass from the  $M_{\text{BH}} - \sigma_*$  (eq. 1; Tremaine et al. 2002) and the  $M_{\text{BH}} - M_{\text{bulge}}$  (eq. 2; Häring & Rix 2004) relations, respectively.

TABLE 2  
DENSITY MODEL FITS TO NGC 6868'S EDGE

Fit range (kpc)	$\alpha_1$	$r_{\text{edge}}$ (kpc)	$J$	$n_1$ ( $10^{-3} \text{ cm}^{-3}$ )	$n_2$ ( $10^{-3} \text{ cm}^{-3}$ )
[7.9, 34.0]	-0.40	22.7	2.2	1.52	0.84
[7.9, 68.0]	-0.15	20.3	1.8	1.47	1.00
[5.8, 34.0]	-0.82	26.5	2.6	1.38	0.66
[5.8, 68.0]	-0.64	22.5	1.7	1.16	0.85

NOTE. — Density models fits across the 0.5–2 keV surface brightness edge in NGC 6868 shown in Figs. 2 and 8 for the density model given in eq. 3.  $n_1$  and  $n_2$  are electron densities inside and outside the edge, respectively, assuming ( $kT, A$ ) of (0.64 keV,  $0.5Z_\odot$ ) and (0.72 keV,  $0.3Z_\odot$ ) inside and to the north outside the edge, respectively. See Table 4.

- Kalberla, P. M. W., Burton, W. B., Hartmann, D., Arnal, E. M., Bajaja, E., Moras, R., Pöppel, W. G. L. 2005, *A & A*, 440, 775  
Koprolin, W. & Zeilinger, W. 2000, *A & AS*, 145, 71  
Kurosawa, R., Proga, D., & Nagamine, K. 2009, arXiv:0906.3739  
Landau, L.D. & Lifshitz, E.M. 1959, *Fluid Mechanics* (London: Pergamon), chapter 9  
Lauer, T., Faber, S., Richstone, D., Gebhardt, K., Tremaine, S., Postman, M., Dressler, A., Aller, M.C., Filippenko, A.V., Green, R., Ho, L.C., Kormendy, J., Magorrian, J. & Pinkney, J. 2007, *ApJ*, 662, 808  
Machacek, M., Dosaj, A., Forman, W.R., Jones, C., Markevitch, M., Vikhlinin, A., Warmflash, A. & Kraft, R.P. 2005a, *ApJ*, 621, 663  
Machacek, M., Nulsen, P.E.J., Stirbat, L., Jones, C. & Forman, W.R. 2005b, *ApJ*, 630, 280  
Machacek, M., Jones, C., Forman, W.R. & Nulsen, P.E.J. 2006, *ApJ*, 644, 155  
Machacek, M.E., Kraft, R.P., Ashby, M.L.N., Evans, D.A., Jones, C. & Forman, W.R. 2008, *ApJ*, 674, 142  
Madejsky, R. & Bien, R. 1993, *A&A*, 280, 383  
Marconi, A. & Hunt, L.K. 2003, *ApJ*, 589, L21  
Magorrian, J., Tremaine, S., Richstone, D., Bender, R., Bower, G., Dressler, A., Faber, S.M., Gebhardt, K., Green, R., Grillmair, C., Kormendy, J. & Lauer, T. 1998, *ApJ*, 115, 2285  
Markevitch, M., Vikhlinin, A., & Mazzotta, P. 2001, *ApJ*, 562, L153  
Markevitch, M. & Vikhlinin, A. 2007, *Physics Reports*, 443, 1  
Matsushita, K., Finoguenov, A., & Böhringer, H. 2003, *A&A*, 401, 443  
Mauch, T., Murphy, T., Buttery, H. J., Curran, J., Hunstead, R. W., Piestrzynski, B., Robertson, J. G., & Sadler, E. M. 2003, *MNRAS*, 342, 1117  
Maughan, B.J., Ellis, S. C., Jones, L.R., Mason, K.O., Cordova, F.A., & Priedhorsky, W. 2006, *ApJ*, 640, 219  
Mazzotta, P. & Giacintucci, S. 2008, *ApJ*, 675, L9  
Mazzotta, P., Edge, A.C., & Markevitch, M. 2003, *ApJ*, 596, 1  
McNamara, B., et al. 2000, *ApJ*, 534, L135  
McNamara, B.R., Nulsen, P.E.J., Wise, M.W., Rafferty, D.A., Carilli, C., Sarazin, C.L., & Blanton, E.L. 2005, *Nature*, 433, 45  
Moore, B., Katz, N., Lake, G., Dressler, A., & Oemler, A. 1996, *Nature*, 379, 613  
Nulsen, P.E.J. 1982, *MNRAS*, 198, 1007  
Nulsen, P.E.J., David, L.P., McNamara, B.R., Jones, C., Forman, W.R. & Wise, M.W. 2002, *ApJ*, 568, 163  
Nulsen, P. E. J.; Hambrick, D. C.; McNamara, B. R.; Rafferty, D.; Birzan, L.; Wise, M. W.; David, L. P. 2005, 625, L9  
Nulsen, P. E. J.; McNamara, B. R.; Wise, M. W.; David, L. P. 2005, *ApJ*, 628, 629  
Osmond, J. P. F. & Ponman, T. J. 2004, *MNRAS*, 350, 1511  
Osmond, J.P.F., Ponman, T.J., & Finoguenov, A. 2004, *MNRAS*, 355, 11  
O'Sullivan, E., Forbes, D. A., & Ponman, T. J. 2001, *MNRAS*, 328, 461  
O'Sullivan, E., Vrtilik, J.M., Kempner, J.C., David, L.P., & Houck, J.C. 2005, *MNRAS*, 357, 1134  
Quilis, V., Moore, B., & Bower, R. 2000, *Science*, 288, 177  
Randall, S., Nulsen, P.E.J., Forman, W.R., Jones, C., Machacek, M., Murray, S.S. & Maughan, B. 2008, *ApJ*, 688, 208  
Randall, S., Jones, C., Markevitch, M., Blanton, E.L., Nulsen, P., Forman, W.R. 2009, *ApJ*, in press, eprint arXiv:0904.0610  
Rangarajan, F.V.N., Fabian, A.C., Forman, W.R., & Jones, C. 1995, *MNRAS*, 272, 665  
Rasmussen, J. & Ponman, T.J. 2007, *MNRAS*, 380, 155  
Ruderman, M. A., & Spiegel, E.A. 1971, *ApJ*, 165, 1  
Scharf, C.A., Zurek, D.R., & Bureau, M. 2005, *ApJ*, 633, 154  
Silk, J. & Rees, M.J. 1998, *A&A*, 331, L1  
Slee, O. B., Sadler, E. M., Reynolds, J. E., & Ekers, R. D. 1994, *MNRAS*, 269, 928  
Smith, R.K., Brickhouse, N.S., Liedahl, D. A. & Raymond, J.D. 2001, *ApJ*, 556, L91  
Tonry, J. L., Dressler, A., Blakeslee, J.P., Ajhar, E. A., Fletcher, A. B., Luppino, G. A., Metzger, M. R., & Moore, C. B. 2001, *ApJ*, 546, 681  
Tittley, E.R. & Henriksen, M. 2005, *ApJ*, 618, 227  
Tremaine, S., Gebhardt, K., Bender, R., Bower, G., Dressler, A., Faber, S. M., Filippenko, A. V., Green, R., Grillmair, C., Ho, L. C., et al. 2002, *ApJ*, 574, 740  
Verdoes Kleijn, G., van der Marel, R.P., Noel-Storr, J. 2006, *AJ*, 131, 1961  
Veron-Cetty, M.-P. & Veron, P. 1988, *A & A*, 204, 24  
Vikhlinin, A., Markevitch, M. & Murray, S.S. 2001, *ApJ*, 551, 160  
Wegner, G., Bernardi, M., Willmer, C. N. A., da Costa, L. N., Alonso, M. V., Pellegrini, P. S., Maia, M. A. G., Chaves, O. L., and Rite, C. 2003, *AJ*, 126, 2268  
Young, A.J., Wilson, A.S., & Mundell, C.G. 2002, *ApJ*, 579, 560  
Zeilinger, W.W., Pizzella, A., Amico, P., Bertin, G., Bertola, F., Buson, L.M., Danziger, I.J., Dejonghe, H., Sadler, E.M., et al. 1996, *A & AS*, 120, 257

TABLE 3  
NGC 6868 SPECTRAL REGIONS ACROSS THE EDGE

label	shape	center (RA, Dec)	radius <sup>a</sup> (arcsec)	angle (deg)
NEdge <sub>-1</sub>	elliptical sector	20 : 09 : 54.1, -48 : 22 : 46.4	82.4, 131.9	6
NEdge <sub>+0</sub>	elliptical sector	20 : 09 : 54.1, -48 : 22 : 46.4	131.9, 211.	6
NEdge <sub>+1</sub>	elliptical sector	20 : 09 : 54.1, -48 : 22 : 46.4	211., 337.6	6
S <sub>+1</sub>	elliptical sector	20 : 09 : 54.1, -48 : 22 : 46.4	211., 337.6	6

NOTE. — NEdge regions are concentric to the bounding ellipse and lie within the sector shown in Fig. 7 and described in §4.1. S<sub>+1</sub> uses the same elliptical annulus as NEdge<sub>+1</sub> but is constrained to lie between 213° and 327.5° (to the south). All angles are measured counter-clockwise from west. Coordinates are J2000. <sup>a</sup> Radii are semi-minor inner (outer) radii for elliptical annular sectors.

TABLE 4  
NGC 6868 SPECTRAL MODELS ACROSS THE EDGE

region	counts (keV)	$kT$ ( $Z_{\odot}$ )	$A$	$\Gamma$	$\chi^2/\text{dof}$	( $\Lambda^a$ )
NEdge <sub>-1</sub>	313	$0.65^{+0.6}_{-0.7}$	0.3	...	11.6/19	6.2
NEdge <sub>-1</sub>	313	$0.65 \pm 0.07$	0.5	...	11.2/19	9.2
NEdge <sub>-1</sub>	313	$0.64 \pm 0.08$	0.5	1.6	10.5/18	9.2
NEdge <sub>-1</sub>	313	$0.66 \pm 0.06$	1.0	...	11.1/19	16.8
NEdge <sub>+0</sub>	286	$0.71^{+0.08}_{-0.11}$	0.2	...	30.2/31	4.7
NEdge <sub>+0</sub>	286	$0.72^{+0.08}_{-0.11}$	0.3	...	30.6/31	6.1
NEdge <sub>+1</sub>	464	$0.73^{+0.07}_{-0.09}$	0.3	...	65.7/55	6.1
NEdge <sub>+1</sub>	464	$0.69^{+0.08}_{-0.10}$	$0.11^{+0.13}_{-0.10}$	...	61.7/54	3.3
S <sub>+1</sub>	691	$0.63^{+0.05}_{-0.06}$	$0.29^{+0.24}_{-0.18}$	...	72.1/68	6.1

NOTE. — Spectral models are an absorbed APEC model or absorbed APEC + power law model. Hydrogen absorption is fixed at the Galactic value ( $N_{\text{H}} = 3.9 \times 10^{20} \text{ cm}^{-2}$ , Kalberla et al. 2005). Parameters without 90% CL uncertainties are fixed. <sup>a</sup>  $\Lambda$  is the X-ray emissivity in the 0.5–2 keV energy band in units of  $10^{-15} \text{ photon cm}^3 \text{ s}^{-1}$ .

TABLE 5  
NGC 6868 EDGE ANALYSIS

case <sup>a</sup>	$T_1/T_2$	$(\Lambda_1/\Lambda_2)^{1/2}$	$n_1/n_2$	$p_1/p_2$	Mach	velocity ( $\text{km s}^{-1}$ )
1	0.89	0.99	1.67–2.56	1.49–2.28	0.72–1.08	318–475
2	0.88	0.81	1.37–2.10	1.21–1.85	0.47–0.9	207–397
3	0.90	0.60	1.01–1.55	0.90–1.39	0–0.65	0–287

NOTE. — Case (1,2,3) correspond to spectral models given in Table 4 with abundances inside the edge of (0.3,0.5,1.0), respectively, and temperature, abundance and sound speed outside the edge of 0.72 keV,  $0.3Z_{\odot}$  and  $440 \text{ km s}^{-1}$ .

TABLE 6  
NGC 6868 SPECTRAL REGIONS FOR TEMPERATURE MAP FEATURES

label	shape	center (RA, Dec)	radius <sup>a</sup> (arcsec)	angle (deg)
T <sup>b</sup>	ellipse	20 : 10 : 13.3, -48 : 27 : 16.1	196, 105	333
	ellipse	20 : 09 : 40.0, -48 : 27 : 02.4	149.6, 92.8	21.5
F	ellipse	20 : 09 : 45.4, -48 : 24 : 27.0	150., 62.7	29.2
C	circle	20 : 10 : 04.9, -48 : 22 : 54.4	72.5	...
N	circle	20 : 09 : 53.7, -48 : 22 : 46.6	6.2	...

NOTE. — All angles are measured counter-clockwise from west. Coordinates are J2000. <sup>a</sup> radii are semi-(major,minor) axes for ellipses and radius for circles  
<sup>b</sup> T is the sum of the two elliptical regions given.



TABLE 7  
NGC 6868 SPECTRAL MODELS FOR TEMPERATURE MAP FEATURES

region	counts (keV)	$kT$ ( $Z_{\odot}$ )	$A$	$\Gamma$	$\chi^2/\text{dof}$
T	785	$0.62 \pm 0.04$	$0.4^{+1.07}_{-0.20}$	...	79.0/79
F	607	$0.71 \pm 0.05$	0.3	...	37.3/37
F	607	$0.70 \pm 0.05$	0.2	...	35.2/37
C	504	$0.59^{+0.04}_{-0.05}$	0.5	...	38.2/28
N	790	$0.63^{+0.07}_{-0.06}$	1.0	1.6	37.7/31
N	790	$0.63^{+0.07}_{-0.06}$	1.0	1.4	32.1/31
N	790	$0.63^{+0.07}_{-0.06}$	1.0	2.0	51.9/31

NOTE. — Spectral models are an absorbed APEC model or absorbed APEC + power law. Hydrogen absorption is fixed at the Galactic value  $N_{\text{H}} = 3.9 \times 10^{20} \text{ cm}^{-2}$ , (Kalberla et al. 2005). Parameters without 90% CL uncertainties are fixed.

TABLE 8  
NGC 6861 SPECTRAL REGIONS

label	shape	center (RA, Dec)	radius <sup>a</sup> (arcsec)	angle (deg)
E	rectangle	20 : 07 : 51.8, -48 : 22 : 01.0	284.7, 392.3	0
G	ellipse	20 : 07 : 19.5, -48 : 22 : 12.9	31.6, 19.4	33.8
FA <sup>b</sup>	annular sector	20 : 07 : 19.5, -48 : 22 : 12.9	39.9, 106.8	...
WT	rectangle	20 : 07 : 01.6, -48 : 22 : 13.7	281.4, 269.6	0
NW	rectangle	20 : 07 : 14.3, -48 : 17 : 46.5	372.8, 147.2	47.3

NOTE. — Angles are measured counter-clockwise from west. Coordinates are J2000. <sup>a</sup> radii are (length, width) for rectangles, semi-(major,minor) axes for the ellipse, and (inner,outer) radius for the annular sector. <sup>b</sup> annular region is constrained to lie between  $80^\circ$  and  $282^\circ$  measured counterclockwise from west.

TABLE 9  
NGC 6861 SPECTRAL MODELS

region	source counts	$kT$ (keV)	$A$ ( $Z_{\odot}$ )	$\Gamma$	$\chi^2/\text{dof}$
E1	404	$0.61^{+0.24}_{-0.07}$	$0.027^{+0.04}_{-0.02}$	...	28.5/22
E2	404	$1.26^{+0.44}_{-0.26}$	0.2	...	26.3/21
G	436	$0.52^{+0.17}_{-0.18}$	0.2	...	8.6/16
FA	214	$0.66^{+0.11}_{-0.07}$	0.5	$1.86^{+0.57}_{-0.55}$	10.6/9
WT	621	$1.3^{+0.3}_{-0.2}$	$0.5^{+1.8}_{-0.28}$	...	35.7/42
NW	385	$1.18^{+0.10}_{-0.12}$	$0.25^{+0.21}_{-0.13}$	...	39/28
		$0.90 \pm 0.09$	$0.22^{+0.26}_{-0.11}$	...	

NOTE. — Spectral models are an absorbed APEC thermal plasma model, two component absorbed APEC or absorbed APEC + power law. Hydrogen absorption is fixed at the Galactic value  $N_{\text{H}} = 3.9 \times 10^{20} \text{ cm}^{-2}$ , (Kalberla et al. 2005). Parameters without 90% CL uncertainties are fixed.